nature aging

TECHNICAL REPORT

https://doi.org/10.1038/s43587-021-00134-3

Profiling epigenetic age in single cells

Alexandre Trapp, Csaba Kerepesi and Vadim N. Gladyshev ✉

DNA methylation dynamics have emerged as a promising biomarker of mammalian aging, with multivariate machine learning models ('epigenetic clocks') enabling measurement of biological age in bulk tissue samples. However, intrinsically sparse and binarized methylation profiles of individual cells have so far precluded the assessment of aging in single-cell data. Here we introduce *scAge*, a statistical framework for epigenetic age profiling at single-cell resolution, and validate our approach in mice. Our method recapitulates the chronological age of tissues while uncovering heterogeneity among cells. We show accurate tracking of the aging process in hepatocytes, demonstrate attenuated epigenetic aging in muscle stem cells and track age dynamics in embryonic stem cells. We also use *scAge* to reveal, at the single-cell level, a natural and stratified rejuvenation event occurring during early embryogenesis. We provide our framework as a resource to enable exploration of epigenetic aging trajectories at single-cell resolution.

Aging is characterized by several canonical hallmarks, including epigenetic alterations at CG dinucleotides (CpG sites)[1,2]. Changes in CpG methylation with age can now be assayed using a variety of approaches, ranging from hybridization arrays to genome-wide or targeted next-generation sequencing methods[3–7]. These techniques enable quantitative examination of the dynamic DNA methylation landscape at single-base resolution in the tissues of organisms, such as mammals, that evolved this type of regulation.

Since their inception in the past decade, predictive multivariate machine learning models based on DNA methylation (DNAm) levels, termed 'epigenetic clocks' have revolutionized the aging field[4,8–12]. First built strictly as estimators of chronological age, these clocks can now also integrate and predict various measures of biological aging and disease risk, underscoring their clinical relevance[13–15]. Excitingly, several pan-tissue mammalian clocks recently developed can profile epigenetic age in virtually any tissue across eutherians with remarkable precision, suggesting strong conservation of epigenetic aging patterns across species[16]. Epigenetic clocks are also of keen interest within the fields of lifespan extension and cell reprogramming, as many of these models detect changes in biological age resulting from these interventions[11,12,17–21].

However, while individual cells are the units of life, all existing epigenetic clocks rely on measurements derived from bulk samples (that is, samples containing many cells), for both the creation and application of these models[19]. Historically, the use of bulk samples for DNA methylation analysis has been an inherent requirement of the methodologies available, which demanded large amounts of input DNA material due to degradation of nucleic acids during bisulfite conversion[22]. While the use of bulk samples enables analyses of average methylation patterns in tissues, it simultaneously obscures the epigenetic heterogeneity that exists among individual cells[19,23]. A recent study characterized the transcriptomic changes in murine aging at single-cell resolution, but age-associated CpG methylation changes in single cells of mammals remain mostly unexplored[24].

Advances in epigenomic sequencing methods have now made it possible to evaluate limited methylation profiles in single cells. Since the inception of these techniques in the previous decade, a variety of methods have surfaced, including single-cell whole-genome[23,25] and reduced-representation bisulfite sequencing (RRBS)[26]. Excitingly, approaches for measurement of gene expression, DNA methylation and chromatin accessibility in the same single cell have recently surfaced, allowing for robust integration of multiomic analyses and comprehensive characterization of individual cell states[27–30].

Despite this remarkable progress in single-cell omics, intrinsic issues of sparsity remain. In the case of whole-genome methylation profiling, only a small fraction of CpGs covered with bulk sequencing methods can currently be assayed at once in any single cell[25]. Furthermore, the most widespread protocols for single-cell methylome profiling—those involving genome-wide interrogation of DNA methylation patterns—suffer additionally from effectively random coverage of reads[22]. Several robust imputation and clustering strategies have been developed to address this constraint, employing Bayesian or deep learning approaches to fill in missing methylation states for CpGs not covered in any given cell[31,32]. However, these tools require building complex, time-intensive, dataset-specific models, which may introduce some bias.

This sparsity in single-cell DNAm profiles poses profound limitations for the creation of single-cell epigenetic clocks. Building these predictive models has traditionally relied on collection of methylation levels of CpGs covered consistently across samples of different ages[4,11,12,33,34]. In bulk tissue, this enables the assembly of large methylation matrices that can be directly harnessed for machine learning, particularly elastic net regularization[35]. Currently, however, sparse and binarized methylation profiles of single cells severely complicate the use of this conventional approach[19].

Here we report *scAge*, an epigenetic clock framework capable of profiling biological age at single-cell resolution. Due to inconsistent CpG coverage between cells, our approach instead employs a ranked intersection algorithm that is independent of which CpGs are covered in each cell. By harnessing the relationship of methylation levels with age in a subset of CpGs, we compute a likelihood profile that quantifies the epigenetic age of a cell. Our method recapitulates the chronological age of tissues while also uncovering the intrinsic epigenetic heterogeneity that exists among individual cells. We anticipate that the use of these epigenetic clock approaches may open up exciting new avenues for ultra-low-input organismal age profiling, as well as research on biological aging at the previously elusive level of single cells.

Division of Genetics, Department of Medicine, Brigham and Women's Hospital, Harvard Medical School, Boston, MA, USA. ✉e-mail: vgladyshev@rics.bwh.harvard.edu

Results

Designing *scAge*: a single-cell epigenetic clock framework. Major challenges in the assessment of epigenetic age in single cells are their sparse and binarized methylation profiles. Contrary to bulk samples, sequence reads typically cover different parts of the genome of each single cell (Fig. 1a). This results in limited overlap among cell profiles, particularly with genome-wide methods, precluding the use of conventional elastic net approaches that rely on consistent CpG coverage across samples (Supplementary Fig. 1). To overcome these limitations, we introduce *scAge*, a framework for profiling of epigenetic age using single-cell methylation data (Fig. 1b–e). To develop this single-cell clock approach, we first assumed that the methylation levels of highly covered CpG sites in bulk sequencing or DNAm array profiling of a tissue offer an estimation of the probability of binary methylation at these particular CpG sites in any single cell derived from this tissue. Hence, if we measure a bulk methylation level of 0.7 at a single CpG and pick a random single cell from this tissue, we can assume that there is a 70% chance this particular cell will be methylated at this locus. Using training data derived from highly covered bulk RRBS, we generated reference datasets of deterministic linear models that estimate the average change in methylation levels based on chronological age for each CpG.

Next, to overcome the intrinsic sparsity of single-cell methylomes, we designed a ranked intersection algorithm that isolates the common CpG sites between any single-cell profile and a reference dataset (Fig. 1c). From this common set of sites we selected the most age-associated CpGs, ranking them based on the absolute magnitude of their Pearson correlation with age in the bulk training data. Since different CpG sites are covered in each cell, a distinct collection of age-associated CpGs is chosen by the algorithm per individual cell. For each selected age-associated CpG site we computed the probability of observing a methylated or unmethylated state in a single cell for each age within a wide range (Fig. 1d). In essence, we compare the methylation status (0, unmethylated versus 1, methylated) of the single cell with the estimate from the bulk-derived linear regression model, and use the difference between the model's prediction and the single-cell methylation value as a probability estimate. Our method inherently leverages the notion that if bulk methylation at a certain CpG increases with age, we expect to find more cells methylated at this locus in aged tissues compared to young ones and, conversely, if methylation shows an opposing trend.

To obtain a single probability value for each age assessed by our algorithm, we first assume that binary methylation states of all CpGs in a single cell are independent, and multiply the CpG-wise probabilities together to obtain the overall likelihood of observing the entire filtered age-associated methylation profile. Practically, we calculate this via logarithmic sums rather than fractional products to circumvent underflow errors. Finally, following generation of an age-likelihood distribution for each cell, we assign the age of maximum likelihood as the predicted epigenetic age for this cell (Fig. 1e). We found that this framework, which we designate *scAge*, permits accurate epigenetic age profiling in single cells with dramatically different and sparse methylome profiles. To assess epigenetic age in murine single cells, we trained linear model reference datasets using filtered bulk RRBS methylation matrices from C56BL/6J mice of different ages in three individual tissues (liver, blood and muscle), as well as with a multi-tissue matrix (Fig. 2a and Extended Data Figs. 1 and 2)[34].

scAge tracks aging in hepatocytes and embryonic fibroblasts. We first applied *scAge* to a dataset of 26 single cells, consisting of 11 hepatocytes from 4-month-old mice, ten hepatocytes from 26-month-old mice and five mouse embryonic fibroblasts (MEFs) (Fig. 2b)[23]. Due to inherently random and sparse coverage, single-cell methylome profiles contained limited common CpGs between any given pair of cells; in fact, this effect was greatly accentuated when sites in all cells were progressively intersected, leading to minimal final overlap (Fig. 2c).

Coverage varied widely among the cells, ranging from 0.4 to >8 million CpGs per cell (Extended Data Fig. 3a). Mean methylation was consistent between young and old hepatocytes, but MEFs showed nominally decreased global methylation compared to both groups of hepatocytes (Fig. 2d). We applied our *scAge* framework, trained on liver, blood or multi-tissue datasets, to profile epigenetic age in all 26 cells (Extended Data Fig. 3b,c). Our tool produced distinct likelihood distributions for each cell, enabling quantification of predicted epigenetic age and confidence intervals in a cell-specific manner (Extended Data Fig. 4 and Supplementary Fig. 2). As expected, the liver-trained model showed the highest accuracy with a Pearson correlation coefficient of 0.88 based on the hepatocyte data. The multi-tissue model showed a significant difference between young and old hepatocytes but was less robust, with Pearson $r = 0.63$. Interestingly, application of scAge trained exclusively on blood samples to this data showed no significant difference in the predicted ages of both groups of hepatocytes. This suggests the presence of tissue-specific methylation trajectories, and indicates that *scAge* is likely to be most accurate when trained on the tissue from which the single cells of interest originate. With all models, MEFs displayed the lowest predicted epigenetic age, trending towards 0 in both liver and multi-tissue clocks.

Interestingly, the highly accurate liver *scAge* model predicted the epigenetic age of one hepatocyte in the young group to be around 20 months. This hepatocyte, along with another cell in the old group, were identified as outliers in the original paper[23]. Both cells

Fig. 1 | Designing the *scAge* framework. a, Schematic representation of the distinction between single-cell and bulk methylation sequencing outputs. With bulk approaches (right), read coverage is high and consistent between samples. In single cells (left), read coverage is low (often 1) and inconsistent between single cells, resulting in limited, distinct methylome profiles. **b**, Schematic representation of the *scAge* framework. The input (left) consists of binary single-cell methylome profiles coupled with a training reference dataset constructed from bulk samples across a wide age range (top). In turn, the algorithm outputs epigenetic age predictions for each single cell (right). **c**, Schematic of the intersection and ranking components of the framework. Left, binary single-cell profiles are intersected with a bulk reference, and only CpGs that are common between a particular single cell and the reference data are retained. Right, a ranking step is implemented that orders and selects CpGs based on their absolute Pearson correlation $|r|$ with age. Common CpGs are filtered depending on the chosen parameter, producing binary matrices of age-associated CpG sites for each single cell (bottom). Different CpGs are denoted by letters (z, p, f, b, etc.). **d**, Schematic of the probability computation step of the framework. Linear regression equations relating methylation and age are computed based on bulk data (purple line). Using the observed methylation status of a cell (methylated, orange; unmethylated, green), the probability of observing a particular state is computed as 1 minus the distance between the binary methylation status and the regression line estimate for a particular age. **e**, Schematic of the maximum likelihood estimation step of the framework. In theory, the product of individual CpG probabilities (left) is taken (assuming independence between CpGs), generating a single probability value for each age. Practically, these fractional products are replaced by logarithmic sums to circumvent underflow errors in computation. An age-likelihood distribution is then obtained for every cell (right), and the age of maximum likelihood is interpreted as the epigenetic age of the cell (blue, young cell; red, old cell). Prk denotes the methylation probability for a specific CpG k at a particular age, summed from 1 CpG up to *N* total CpGs.

are also identified as 'very old' outliers using the multi-tissue model. Since coverage was relatively high in these cells, we hypothesized that our results may be reflective of an accelerated aging trajectory (that is, senescence; Extended Data Fig. 5a). This is supported by the global hypomethylation observed in these cells compared to others in the study, which is known to be a factor of senescence progression (Extended Data Fig. 5b)[36]. While senescence may explain the aberrant epigenetic age predictions for these cells, dimensionality reduction performed in the original study[23] classifies these two cells as clear outliers, which may simply suggest that these predictions result from aberrant methylation profiles caused by technical artifacts during isolation or sequencing.

When these two outliers were removed from the analysis, the accuracy of liver and multi-tissue clocks increased drastically, with Pearson $r = 0.95$ (median absolute error = 2.1 m) and 0.86 (median absolute error = 4.5 m), respectively (Fig. 2e). Outlier removal also induced a marginally significant difference between MEFs and young hepatocytes across both models (Fig. 2f). Regardless of whether these outlier cells are included or not, we observed no significant relationship between predicted epigenetic age computed

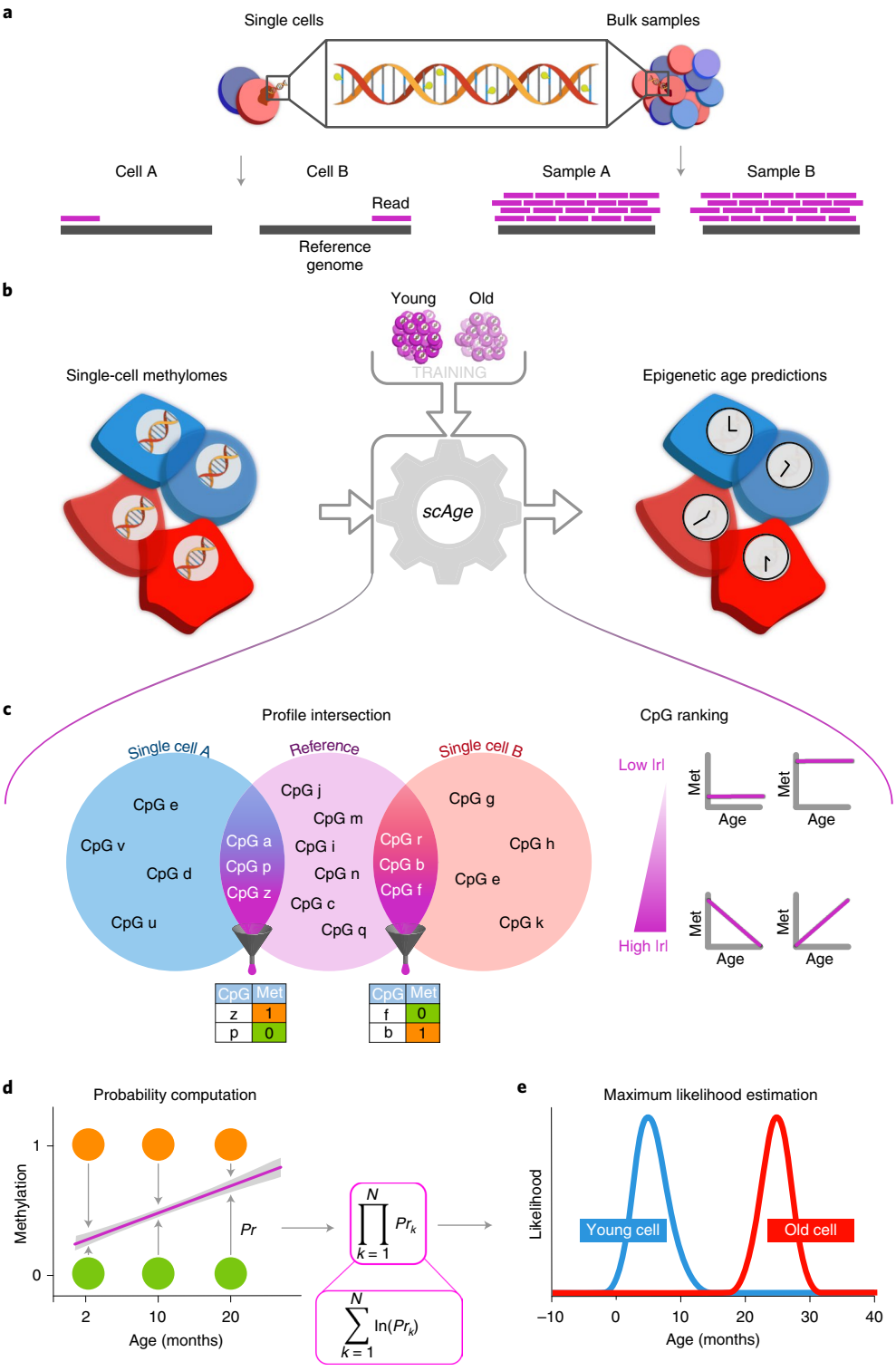

by any of three models and either mean global methylation or total CpG coverage (Extended Data Fig. 5c,d). Recent liver-specific and multi-tissue clocks built using elastic net regression on bulk murine samples displayed an average error of 2–4 months, comparable to or greater than that observed with our single-cell method[12,37]. In turn, these findings suggest that our prediction framework is accurate and generally robust to the technical variability that can arise from single-cell methylome sequencing.

One of the main parameters of our algorithm is the fraction of age-associated CpGs included in the likelihood profile computed by *scAge* to output a predicted epigenetic age for every cell (Fig. 1c–e). We benchmarked results of the algorithm across two methods for CpG selection. In both cases, we first rank CpGs based on their absolute Pearson correlation with age. Then, the algorithm picks either a defined number *n* of highly ranked CpGs or the top *x* percentage of age-associated CpGs for every cell. Although the results between both selection methods are comparable, we find that the latter method (based on percentiles) better accounts for technical differences in coverage frequently observed in single-cell methylome profiling (Extended Data Fig. 6). Interestingly, with either mode, we find that increasing the number or fraction of CpGs taken as input to the algorithm results in poorer performance when using the liver model, wherein predictions for old hepatocytes progressively decrease in accuracy (Extended Data Fig. 7). For the multi-tissue model we observed a gain in precision as more CpGs were taken as input to the algorithm. We attribute this difference primarily to the distinct distributions of linear association metrics in single- versus multi-tissue training datasets: correlation and regression coefficients are much weaker in the latter (Extended Data Fig. 8).

Muscle stem cells display attenuated epigenetic aging. To investigate the unique applicability of our approach to rare cell populations, we applied *scAge* to young and old muscle stem cell (MuSC) data[38]. This dataset consisted of 136 and 139 MuSCs from 1.5- and 26-month-old B6D2F1/JRj mice, respectively (Fig. 3a). As was done in the original study, we omitted cells with <500,000 CpGs covered to discard low-quality dropout cells; this resulted in a final filtered dataset of 116 young and 89 old MuSC methylation profiles (Extended Data Fig. 9a). Mean methylation was slightly elevated in old cells (Fig. 3b). We computed epigenetic age predictions in these MuSCs using three training models, including muscle, blood and multi-tissue datasets. The muscle and multi-tissue clocks showed a slim but significant increase in epigenetic age between both groups, while the blood clock demonstrated no difference between young and old MuSCs (Fig. 3c). As expected, the muscle-trained model was the most accurate, with the lowest median absolute error compared to the other models. Analysis of the relationship between global methylation and predicted epigenetic age uncovered a small positive correlation between both variables using the muscle and multi-tissue training datasets (Fig. 3d). Furthermore, inclusion of all 275 unfiltered cells for predictions revealed that *scAge* is a robust profiling tool for cells with modest to high coverage, but outputs aberrant and highly variable predictions when coverage is dramatically low (Extended Data Fig. 9b).

Our results are remarkably similar to a previous analysis that employed a pseudobulk grouping approach to overcome the coverage sparsity in single-cell MuSC methylomes[38]. That analysis similarly found a slim increase in epigenetic age on the order of a few weeks, far lower than the ~24-month chronological age difference between the two groups of mice. In turn, both methods, employed independently, suggest that MuSCs display minimal aging as measured by DNA methylation patterns. It is, however, known that MuSCs lose functionality and regenerative capacity with age, partly as a result of autophagy-mediated shifts from prolonged quiescence to irreversible senescence and Hoxa9-dependent activation[39,40]. It was also recently suggested that human MuSCs are refractory to aging, hinting that these cell populations probably have distinct biological aging patterns across mammals compared to differentiated muscle cells[41]. Integrating these functional data with our epigenetic age results may shed light on the complex temporal trajectories that govern MuSC biology. Overall, our results agree with the previously reported epigenetic aging dynamics of MuSCs, but offer enhanced single-cell resolution to the data.

Culture conditions impact embryonic stem cell epigenetic age. We next sought to evaluate *scAge* on single-cell methylation datasets profiling pluripotent embryonic stem cells (ESCs). Using conventional clock approaches, bulk ESC samples and their induced pluripotent stem cell (iPSC) counterparts generally show very low predicted epigenetic ages trending towards zero[4,11,12,20,42]. Of note, ESCs may be cultured under a variety of conditions—most commonly in media supplemented with leukemia inhibitory factor (LIF) and serum, or in serum-free '2i' medium supplemented with LIF and two small-molecule inhibitors of the MEK and GSK3β pathways (Fig. 4a). Culture of cells in 2i medium was previously shown to drive rapid global hypomethylation in ESCs, producing epigenetic profiles concordant with migratory primordial germ cells[43].

As expected, we observed significant global hypomethylation among 2i cells following reanalysis of two datasets[25,27] (Fig. 4b). We profiled epigenetic age in 28 2i ESCs and 85 serum ESCs from these studies with *scAge* trained on liver, blood and multi-tissue datasets. We selected these particular training models for embryonic cells,

Fig. 2 | *scAge* tracks aging in hepatocytes and embryonic fibroblasts. a, Schematic representation of the training scheme for the framework. *scAge* linear regression models were trained on three tissue-specific methylation matrices (liver, muscle and blood) and a multi-tissue matrix. Further information on training dataset composition can be found in Extended Data Fig. 1. **b**, Schematic representation of cells analyzed in this figure. The dataset[23] consisted of 26 cells, including five embryonic fibroblasts, 11 hepatocytes from young animals (4 months old) and ten hepatocytes from old animals (26 months old). **c**, Boxplots depicting progressive intersection of all single-cell profiles[23] ($n = 26$ single cells). The *y* axis shows the number of common CpGs between a certain number of profiles, shown here in log scale. The order of intersection of single-cell profiles was permuted 100 times to generate a distribution for each additional cell added ($n = 100$ intersection sets per box). Color spectrum reflects a gradient on the *x* axis, from few intersections (yellow) to many intersections (purple). **d**, Mean global methylation in all embryonic fibroblasts (green, $n = 5$), young hepatocytes (blue, $n = 11$) and old hepatocytes (red, $n = 10$). Two-tailed Welch's *t*-test with Bonferroni correction was used for statistical testing. **e**, Predicted epigenetic age versus chronological age in young hepatocytes (blue, $n = 10$) and old hepatocytes (red, $n = 9$) across liver (left), multi-tissue (middle) and blood (right) models. Jitter was applied to chronological age, strictly for visualization purposes. Two outliers, one from each group, were removed based on aberrant PCA clustering in the original study[23]. Plots and metrics with outliers are shown in Extended Data Fig. 3b. Pearson correlation (*r*), the associated *P* value (*P*) and median absolute error (*MedAE*) are shown. Two-tailed Pearson correlation analysis was applied for statistical testing, with statistics for each model computed independently without correction. Violin plots depict kernel density estimations, with the median value highlighted by a black line. Dashed lines depict the identity line between scDNAm age and chronological age. **f**, Predicted epigenetic age for MEFs (green, $n = 5$), young hepatocytes (blue, $n = 10$) and old hepatocytes (red, $n = 9$) across liver (left), multi-tissue (middle) and blood (right) models. Dashed lines represent the chronological age of animals (blue, 4 months; red, 26 months). Two-tailed Welch's *t*-test with Bonferroni correction was used for statistical testing. Boxplots highlight median levels and the first and third quartile, with whiskers depicting observations up to 1.5× interquartile range; dots depict individual cells.

based on the notion that conventional mouse clocks built on these sets of tissues have previously shown the capacity to accurately profile epigenetic age in ESCs and iPSCs near zero and/or discern the effect of longevity/reprogramming interventions[11,12,33,37]. Interestingly, we observed remarkably coherent results across the liver and blood clocks, which showed a low epigenetic age close to zero for serum-grown ESCs and significantly increased epigenetic age in 2i ESCs (Fig. 4c). This trend is consistent with a recent analysis of epigenetic aging patterns in ESCs at the bulk level[42]. We observed a strong negative correlation between mean methylation and predicted ages with both of these models, suggesting that large-scale global methylation shifts probably play a role in the predicted epigenetic age of the cell

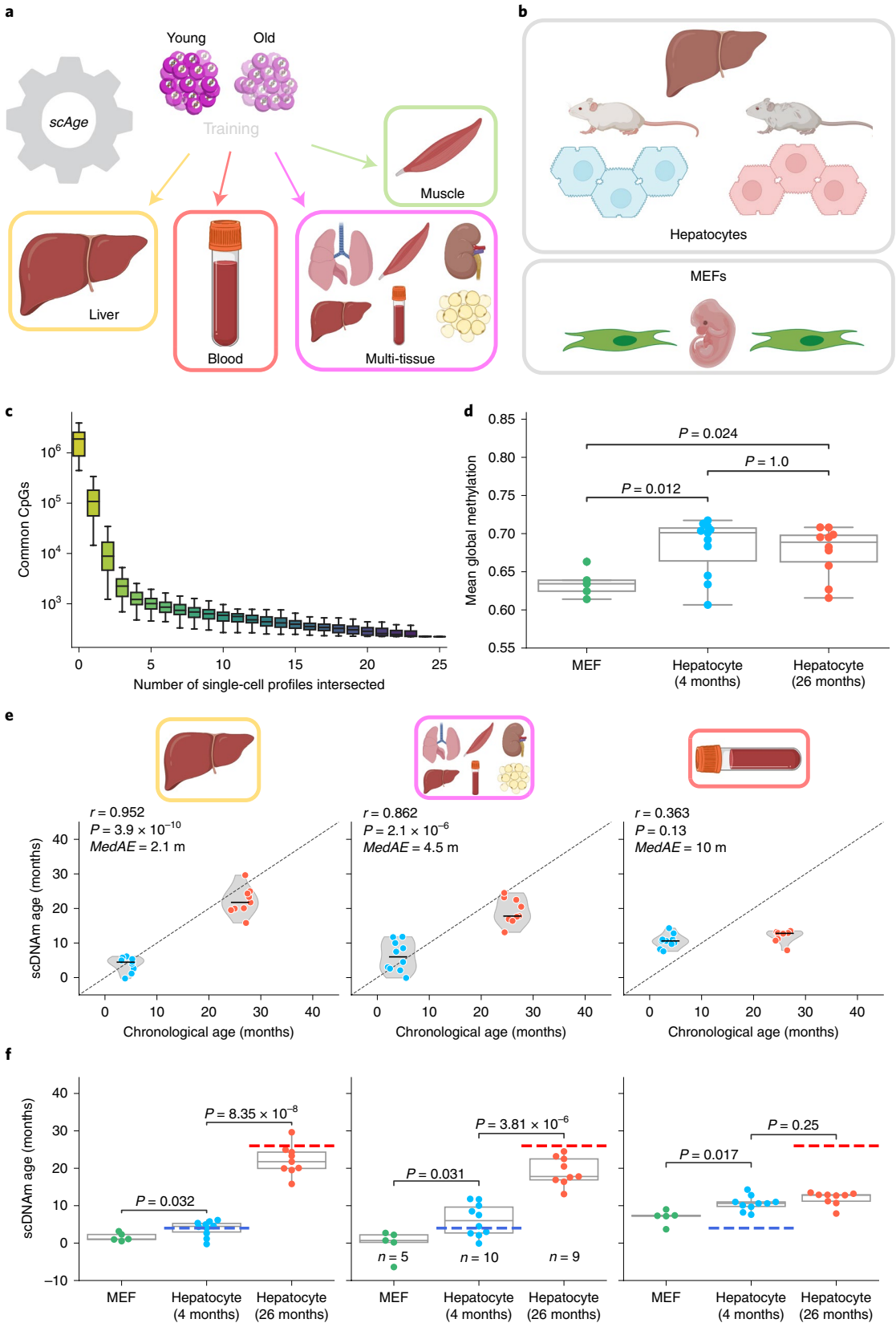

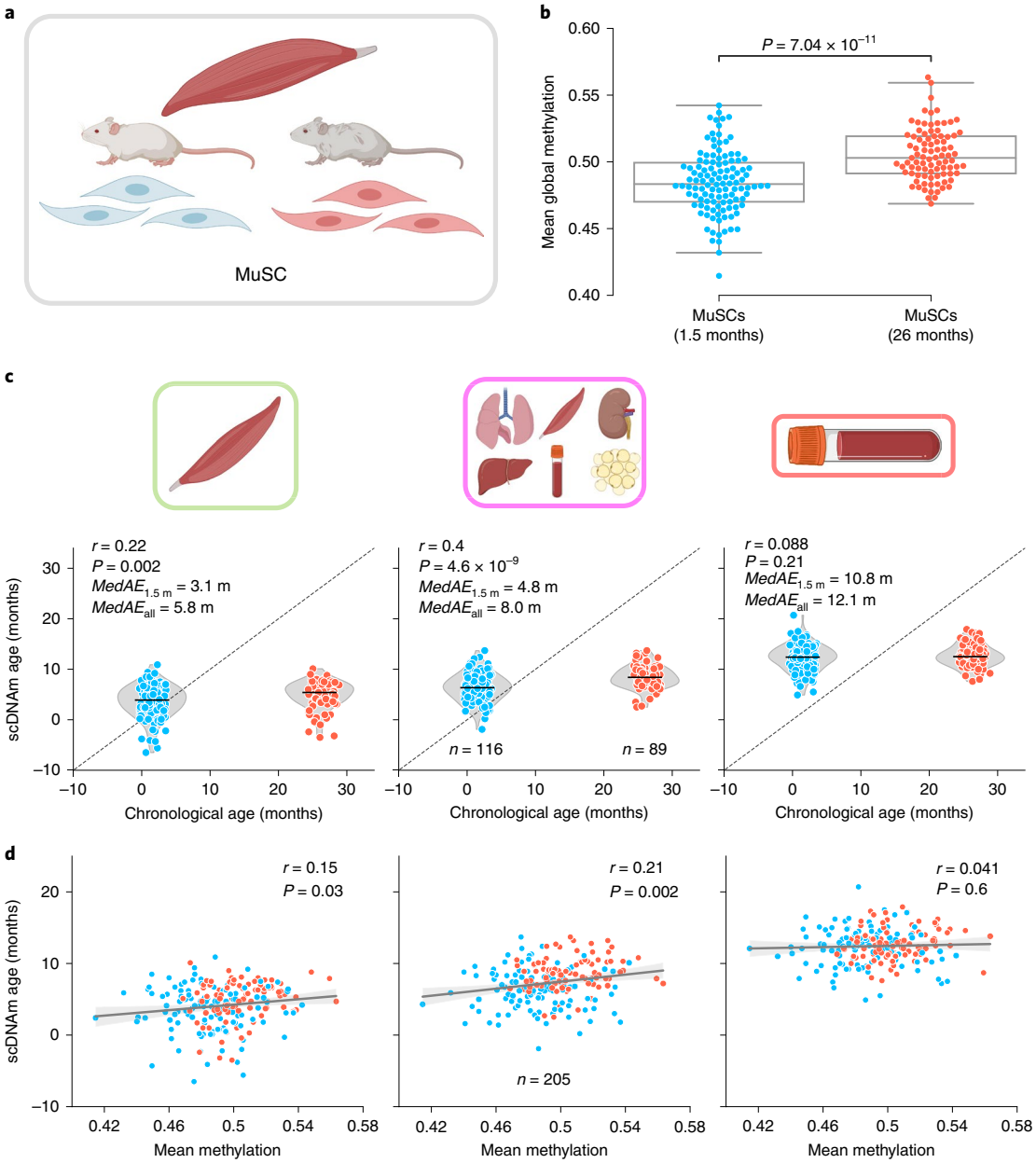

Fig. 3 | MuSCs display attenuated epigenetic aging. a, Schematic representation of cells analyzed[38]. MuSCs were isolated from skeletal muscle tissue of young (1.5 months) and old mice (26 months). Only cells with >500,000 CpGs covered were retained for further analysis. See Extended Data Fig. 9a for additional information. **b**, Mean global methylation in young (blue, $n = 116$) and old (red, $n = 89$) filtered cells. Boxplots highlight median levels and the first and third quartile, with whiskers depicting observations up to 1.5× interquartile range. A single two-tailed Welch's *t*-test was used for statistical testing. **c**, Predicted epigenetic versus chronological age in young (blue, $n = 116$) and old (red, $n = 89$) MuSCs across muscle (left), multi-tissue (middle) and blood (right) models. Median absolute error is shown considering either all cells ($MedAE_{all}$: both 1.5- and 26-month-old cells) or young cells only ($MedAE_{1.5m}$: only 1.5-month-old cells). Jitter on the *x* axis was applied purely for visualization purposes. Pearson correlation (*r*) and the associated *P* value (*P*) are shown. Violin plots depict kernel density estimations of the data, and inner black lines show median predictions. Two-tailed Pearson correlation analysis was used for statistical testing, with statistics for each model computed independently without correction. **d**, Predicted epigenetic age versus mean global methylation for both young (blue) and old (red) MuSCs ($n = 205$) across muscle (left), multi-tissue (middle) and blood (right) models. Regression lines (gray) are shown with 95% confidence intervals (light gray). Two-tailed Pearson correlation analysis was used for statistical testing, with statistics for each model treated independently without correction. Pearson correlation coefficient (*r*) and the associated two-tailed *P* value (*P*) are shown. Individual dots depict single cells throughout the figure.

as assayed by our method (Fig. 4d). The multi-tissue clock profiled low epigenetic ages in both culture conditions but did not detect a significant difference between 2i and serum ESCs.

A stratified rejuvenation event during mouse gastrulation. We then investigated a dataset profiling mouse gastrulation at single-cell resolution, consisting of 758 cells isolated from murine C57BL/6Babr embryos ranging from embryonic day (E) 4.5 to 7.5 (Fig. 5a)[28]. To remove dropout cells with low-quality data, we again discarded those with <500,000 CpGs covered, resulting in a final dataset of 495 single cells across four developmental stages (Extended Data Fig. 9a). Mean global methylation varied drastically

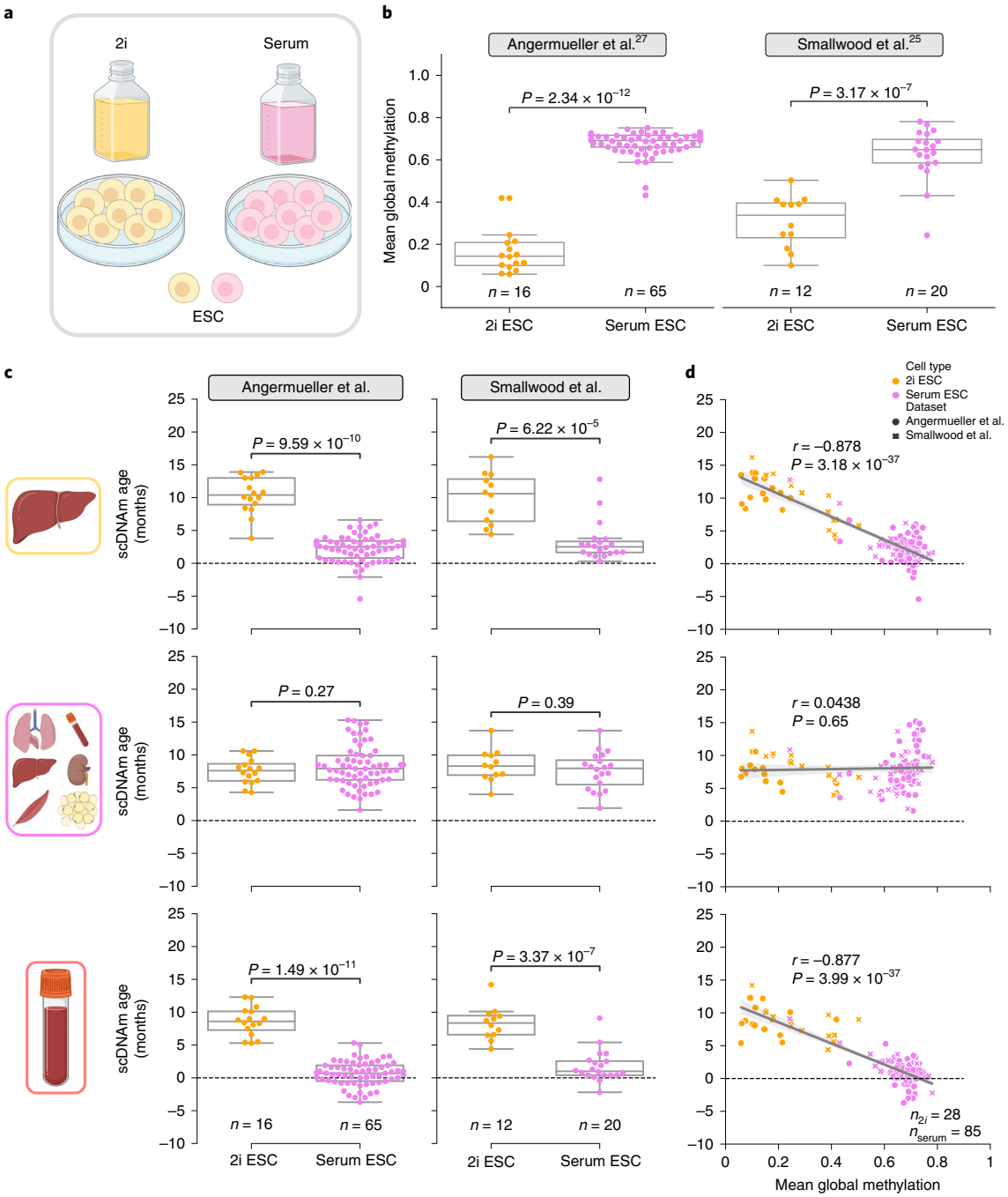

Fig. 4 | Culture conditions influence epigenetic age in single ESCs. a, Schematic representation of single cells analyzed in this figure[25,27]. Cells were grown in medium supplemented with serum, or in serum-free medium with the addition of two small-molecule inhibitors (2i) for the MEK and GSK3β pathways. **b**, Mean global methylation profiles of single ESCs grown under either 2i (yellow, $n_{Angermueller}=16$, $n_{Smallwood}=12$) or serum culture conditions (purple, $n_{Angermueller}=65$, $n_{Smallwood}=20$). Two-tailed Welch's *t*-test was used for statistical testing, with statistics for each dataset treated independently without correction. Boxplots highlight median levels and the first and third quartile, with whiskers depicting observations up to 1.5× interquartile range. **c**, Predicted epigenetic ages in 2i (yellow, $n_{Angermueller}=16$, $n_{Smallwood}=12$) and serum-grown ESCs (purple, $n_{Angermueller}=65$, $n_{Smallwood}=20$) across liver (top), multi-tissue (middle) and blood (bottom) models. Two-tailed Welch's *t*-test was used for statistical testing, with statistics for each model and dataset treated independently without correction. Boxplots highlight median levels and the first and third quartile, with whiskers depicting observations up to 1.5× interquartile range. **d**, Scatterplot relationship between predicted epigenetic age and mean global methylation among all ESCs (yellow, $n_{2i}=28$; purple, $n_{serum}=85$). Regression lines (gray) are depicted with 95% confidence intervals (light gray). Pearson correlation (*r*) and the associated *P* value (*P*) are shown. Two-tailed Pearson correlation analysis was used for statistical testing, with statistics for each model and dataset treated independently without correction. Boxplots show median levels and the first and third quartile, and whiskers show 1.5× interquartile range. Dots depict individual cells, with symbols denoting the study of origin.

during this early period of mouse embryogenesis, with E4.5 cells characterized by global hypomethylation compared to the three subsequent developmental stages (Fig. 5b).

It was recently suggested that embryogenesis may be characterized by an initial decrease in biological age to a point termed 'ground zero', after which organismal aging formally begins[44].

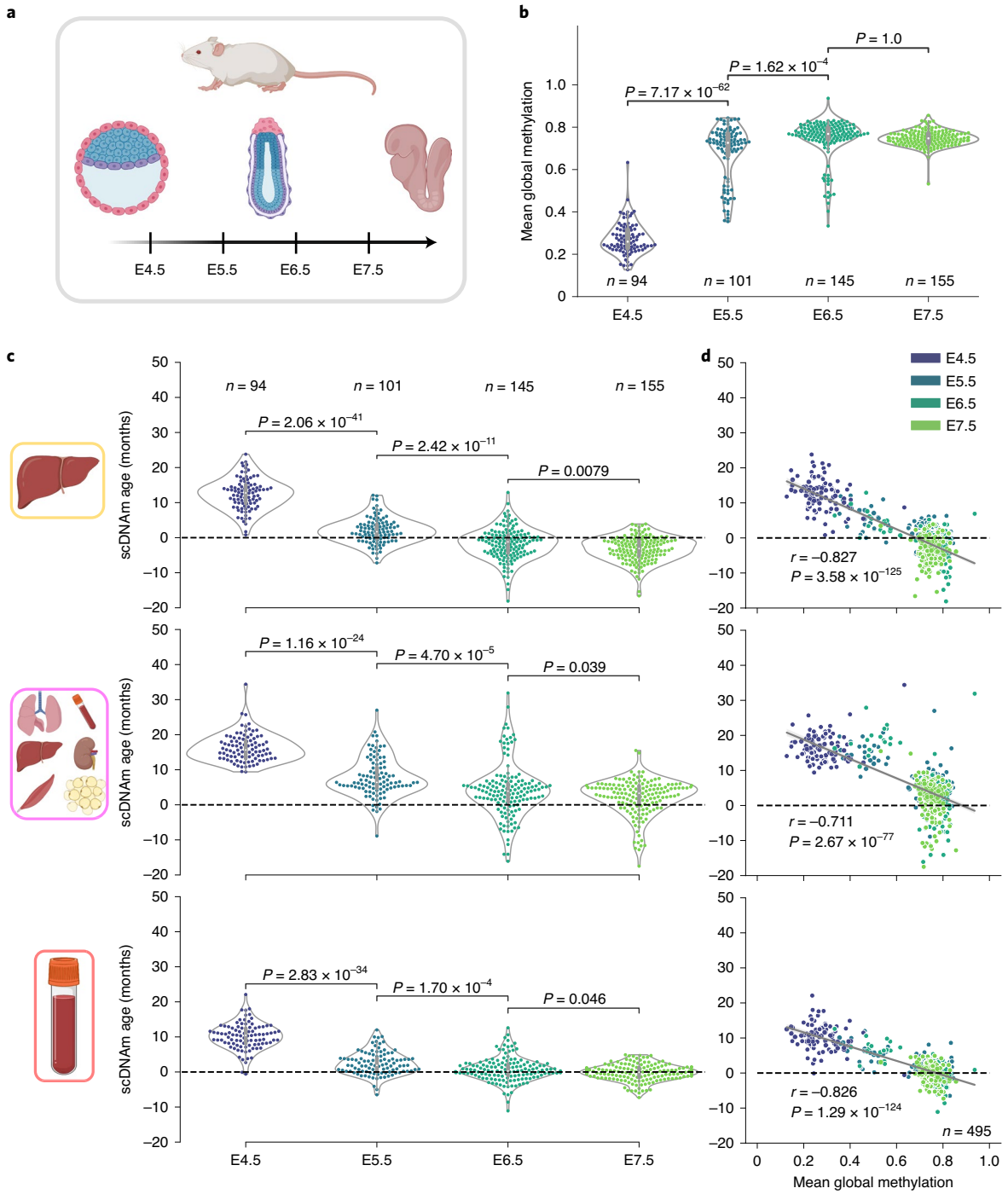

Fig. 5 | An epigenetic rejuvenation event during mouse embryogenesis. a, Schematic representation of cells analyzed in this figure[28]. Single cells from mouse embryos at four developmental stages (E4.5, E5.5, E6.5 and E7.5) were isolated and sequenced. Only cells with at least 500,000 CpGs covered were retained for downstream analysis (see Extended Data Fig. 9a for additional details). **b**, Mean global methylation profiles in single cells across all four developmental stages assayed (purple, $n_{E4.5}=94$; dark blue, $n_{E5.5}=101$; dark green, $n_{E6.5}=145$; light green, $n_{E7.5}=155$). Two-tailed Welch's *t*-test was used for statistical testing, and Bonferroni corrections were applied to correct for multiple testing. Violin plots depict kernel density estimations of the data, and inner boxplots (gray) depict median levels and the first and third quartile, with whiskers extending up to 1.5× interquartile range. Dots depict individual cells. **c**, Predicted epigenetic ages for cells in all four developmental stages ($n_{E4.5}=94$, $n_{E5.5}=101$, $n_{E6.5}=145$, $n_{E7.5}=155$), across liver (top), multi-tissue (middle) and blood (bottom) *scAge* models. Colors correspond to those detailed in **b**. Two-tailed Welch's *t*-test was used for statistical testing, with Bonferroni corrections applied to correct for multiple testing. Violin plots depict kernel density estimate of the data, and inner boxplots (gray) depict median levels and the first and third quartile, with whiskers extending up to 1.5× interquartile range. Dots depict individual cells. **d**, Scatterplot depicting the relationship between mean global methylation and predicted epigenetic age across all cells ($n=495$) in liver (top), multi-tissue (middle) and blood (bottom) models. Colors correspond to those in **b** and in the legend at top right. Regression lines (gray) are depicted with 95% confidence intervals (light gray). Pearson correlation (*r*) and the associated *P* value (*P*) are shown. Two-tailed Pearson correlation analysis was used for statistical testing, with statistics for each dataset treated independently without correction.

Consistent with this idea, recent application of epigenetic clocks to bulk samples revealed a significant reduction in biological age (that is, rejuvenation) during the early stages of embryogenesis, followed by an increase in later stages[42]. This finding also agrees with the notion that damage accumulation inevitably occurs during the lifespan of an organism, even in germ cells. Thus, a rejuvenation event is thought to take place during embryogenesis to ensure the continuous generation of new, biologically young individuals.

To investigate this hypothesis at single-cell resolution, we applied the same *scAge* models used on ESCs to individual embryonic cells from the four developmental stages assayed. Across all models we observed a steady and significant reduction in the predicted age from E4.5 to E7.5, consistent with the notion of a rejuvenation event (Fig. 5c). Interestingly, there was a strong negative correlation across all three models between mean global methylation and predicted epigenetic age (Fig. 5d). This suggests an important association between the de novo methylation event that occurs during embryogenesis and the apparent decrease in biological age.

To further refine the resolution of this rejuvenation event, we integrated lineage information for each cell in the dataset based on precomputed assignments derived from mapping of gene expression patterns of single embryonic cells to a recent atlas of mouse gastrulation (Fig. 6a,b)[28,45]. This increase in resolution revealed that cells mapped to the epiblast lineage accounted for the majority of the rejuvenation signal, showing a strong initial decrease in biological age trending towards or below zero during gastrulation (Fig. 6c). Moreover, newly formed germ layers (endoderm, mesoderm and ectoderm) showed a low biological age near 0. Interestingly, extra-embryonic ectoderm and visceral endoderm cells showed significantly higher predicted ages compared to other embryonic cell types of the same developmental stage. These findings may suggest spatio-temporal stratification of the rejuvenation event; this process may be specific to cells that predominantly go on to form the embryo proper and excludes those fated to become supportive extra-embryonic lineages. Cells failing to show evidence of rejuvenation also retain partially unmethylated profiles (Fig. 6d). This further suggests a deep link between differential demethylation, de novo methylation and the observed lineage-resolved epigenetic age decreases.

Together, these striking results suggest that a stratified rejuvenation event occurs during mid-embryogenesis and that individual cells may be rejuvenated through natural means. The lowest single-cell epigenetic age corresponds approximately to the stage of gastrulation and is associated with de novo hypermethylation, hinting that to rejuvenate cells it may be important to first carefully demethylate and subsequently remethylate the genome.

Discussion

In this work we report scAge, an approach enabling single-cell epigenetic age predictions. Our framework leverages bulk methylation data to train linear models that predict methylation levels from age across a large number of CpG sites. An intersection and ranking algorithm selects informative CpGs covered jointly in a single cell and a reference dataset, followed by computation of a cell-specific likelihood profile across a range of ages. We then assign the age of maximum likelihood as the final epigenetic age of a cell. This method solves the complex challenges of sparse and binarized methylation profiles in single cells, which previously precluded attempts to estimate epigenetic age in individual cells. Indeed, all bulk epigenetic clocks to date require defined sets of CpG sites for their application, an approach that is currently not feasible to employ in the case of single cells.

This method enables accurate age prediction of single hepatocytes and MEFs with high resolution on models trained on liver or multi-tissue datasets. We find that age predictions are most accurate and precise when *scAge* is trained on the tissue to which a particular cell belongs, and that training exclusively on certain other tissues may preclude robust assessment of biological aging; this highlights the importance of tracking tissue- or cell-type-specific epigenetic aging patterns. We also demonstrate that multi-tissue datasets, despite depicting much weaker linear associations with age, are still able to estimate biological age in single cells with reasonable accuracy. This provides utility in the case where the cell type is unknown or if no tissue-specific reference data are available, and may also track tissue-independent CpG methylation trajectories.

Additionally, we show consistency between predictions from our model and previous work in MuSCs, which display attenuated epigenetic aging in comparison to their chronological age. This result, and our single-cell method, offer exciting future avenues for dissecting the role of epigenetic aging and differentiation across mammalian tissues. Particularly, this framework may prove useful in quantification of biological aging in complex differentiation hierarchies and in uncovering the impact of cell state on epigenetic age predictions. We also find that while ESCs are generally predicted to have low epigenetic age, this differs depending on the culture condition and its downstream effect on global methylation patterns. Finally, our data provide further evidence for the recently proposed ground zero hypothesis of aging by showing a strongly significant decrease in the epigenetic age of single cells at the time of gastrulation. We find that this rejuvenation event is stratified, wherein only cells destined for intraembryonic lineages display a significant reduction in epigenetic age.

Despite its utility for single-cell profiling, *scAge* presently has important limitations that need to be acknowledged. For one, binary methylation states of CpGs were here assumed to be completely independent of each other, because previous work suggested that this was the case when analyzing single reads from bulk samples[3,7]. However, a more thorough analysis of this behavior specifically in single cells may reveal biological insights suggesting a more

Fig. 6 | Lineage-specific resolution reveals stratification in the epigenetic rejuvenation event. a, Schematic representation of the transcriptomic mapping procedure used to assign lineage annotations to individual cells, based on multimodal omics data obtained in this study[28] and a reference single-cell gene expression atlas of mouse gastrulation[45]. **b**, Bar plot of the count of different cell lineages across the four developmental stages, based on lineage annotations provided by the authors[28]. Color scale defines the developmental stage (E4.5, purple; E5.5, dark blue; E6.5, dark green; E7.5, light green). **c**, Predicted epigenetic ages for single embryonic cells across liver (top), multi-tissue (middle) and blood (bottom) datasets, grouped by assigned lineage and colored by developmental stage (as detailed in **b**). Number of cells for each lineage-stage pair is shown graphically in **b**: epiblast, $n_{E4.5}=56$, $n_{E5.5}=78$, $n_{E6.5}=94$, $n_{E7.5}=21$; primitive endoderm, $n_{E4.5}=33$; primitive streak, $n_{E6.5}=28$, $n_{E7.5}=19$; endoderm, $n_{E7.5}=24$; mesoderm, $n_{E6.5}=5$, $n_{E7.5}=63$; ectoderm, $n_{E7.5}=27$; visceral endoderm, $n_{E5.5}=23$, $n_{E6.5}=9$; extra-embryonic ectoderm, $n_{E6.5}=8$. Gray-bordered rectangle denotes supportive extra-embryonic tissues that appear not to undergo rejuvenation. Two-tailed Welch's *t*-test was used for statistical testing, and Bonferroni corrections were applied to account for multiple testing. Violin plots depict kernel density estimate of the data, and inner boxplots (gray) depict median levels and the first and third quartile, with whiskers extending up to 1.5× interquartile range. Dots depict individual cells. **d**, Mean global methylation for single embryonic cells grouped by assigned lineage and colored by developmental stage (as in **b**). Number of cells for each lineage-stage pair is shown graphically in **b** and is the same as described in **c**. Gray-bordered rectangle denotes supportive extra-embryonic tissues. Two-tailed Welch's *t*-test was used for statistical testing, and Bonferroni corrections were applied to account for multiple testing. Violin plots depict kernel density estimation of the data and inner boxplots (gray) depict median levels and the first and third quartile, with whiskers extending up to 1.5× interquartile range. Dots depict individual cells. UMAP, uniform manifold approximation and projection.

complex inter-CpG relationship. Additionally, the exclusive use of linear regression may be suboptimal when considering the potentially vast set of mathematical relationships that best model CpG methylation levels and age. In tandem, we observe that some bulk methylation distributions are truncated as a result of their location near the edges of the unit interval, which may have an impact on the creation of linear models and downstream age predictions (Extended Data Fig. 2). Our method also makes use of observed methylation values in bulk data in a deterministic manner to construct linear models, as opposed to random probabilistic modeling of methylation distributions. Despite these limitations, we find that our approach is nevertheless an accurate tool enabling robust epigenetic age profiling in single cells, based on both real single-cell data and simulation analyses (Extended Data Fig. 10).

We note also that we have not explored the effect of cell composition when creating bulk reference datasets. This may be important,

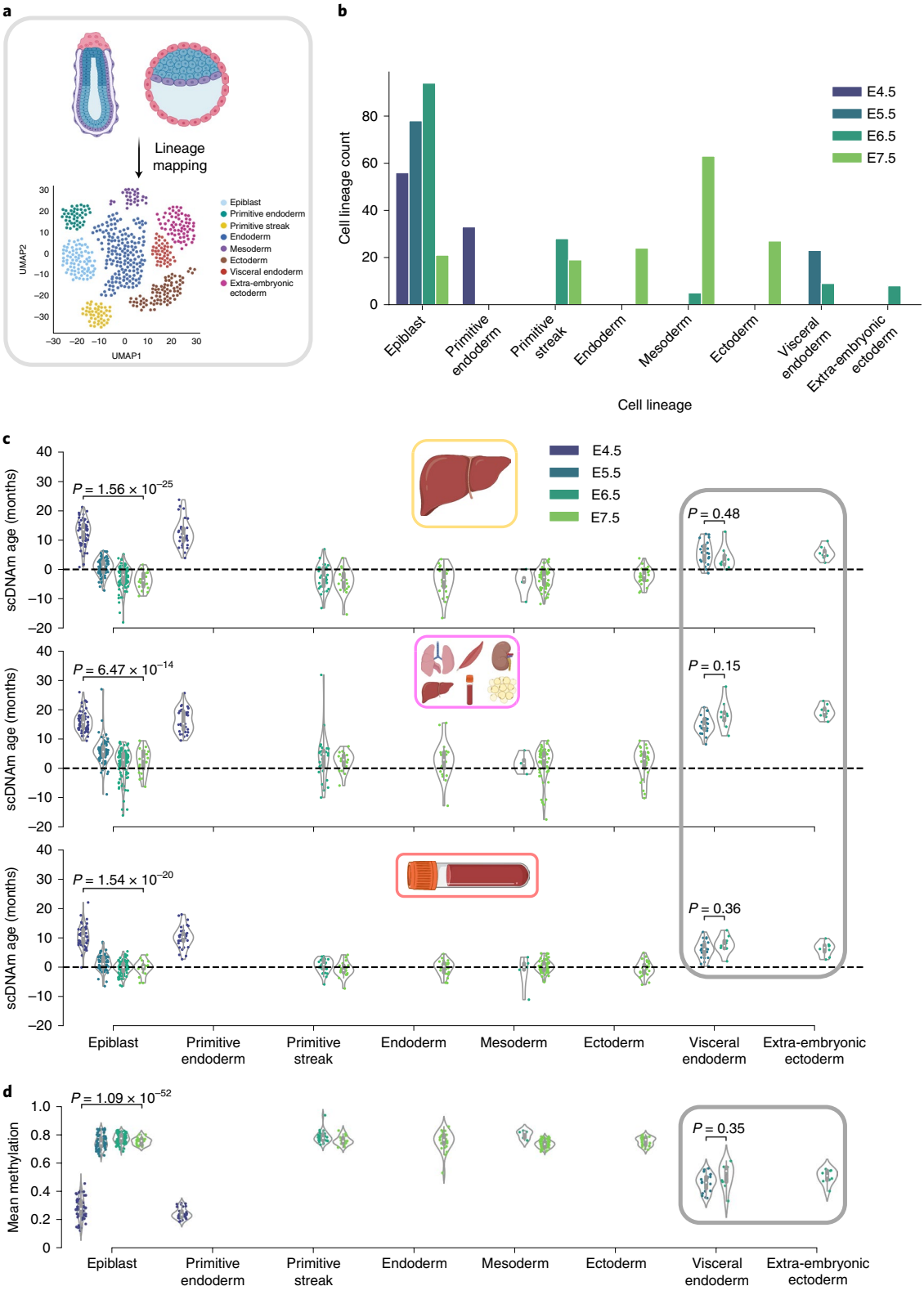

as cell composition is known to change with age in many tissues[1,24]. However, to our knowledge, there are currently no cell-type-specific RRBS mouse methylation datasets with a wide age range that we could use as the input reference dataset of our *scAge* approach, or as input to reference-based, cell-type deconvolution algorithms[46]. Reference-free deconvolution algorithms may hold promise in this regard, but in our testing the lack of definitive cell-type labels, combined with the large influence of age on methylation patterns at critical CpGs, currently precludes the robust use of these techniques[47]. It also remains to be explored how epigenetic age interfaces with differentiation at the cellular level, how individual aging trajectories of cells change with time, how biological age is transferred during events such as mitosis and, finally, how these predictions reflect the fundamental biological state of cells.

Taken together, we find that the aggregation of multiple single-cell predictions provides an accurate average measure of the age of a particular tissue. However, our single-cell clock framework concurrently uncovers some heterogeneity in the aging trajectories of individual cells. It was previously suggested that current bulk epigenetic clocks may function partly by tracking changes in tissue composition with age, and this new approach may serve to elucidate to what extent this occurs at single-cell resolution[4,38]. Our current results hint that some cells may undergo accelerated or decelerated epigenetic aging, which was previously impossible to ascertain. Nevertheless, the age of the majority of differentiated cells was consistent with the age of the tissue, arguing against the idea of altered tissue composition as the sole basis for existing bulk clocks. Thus, *scAge* revealed that individual cell lineages within organisms indeed age.

These findings are particularly in line with recent work that uncovered bulk and single-cell cross-tissue gene expression changes with age in mice[24,48], and with the notions of asynchronous and digital aging recently put forth[49]. *scAge* further showed that certain cells destined to become part of the embryo during the process of gastrulation are naturally rejuvenated. It would be of particular interest to uncover the mechanisms underlying this process, which may form the basis of putative rejuvenation therapies.

Our single-cell approach, *scAge*, may have profound clinical applications for mammalian somatic, germline and cancer cells, as it may be possible to epigenetically discriminate and map 'young' and 'old' cells within heterogeneous tissues via this approach. Additionally, our method may be instrumental in assessing the rejuvenation process following epigenetic reprogramming, as well as in other processes that generate extensive cell-to-cell heterogeneity. We present here a framework to profile epigenetic age in single cells, with exciting applications at the interface of aging, rejuvenation and emerging single-cell technologies.

Methods

Ethics and animals. Our study complies with all relevant ethical regulations. We used publicly available datasets of murine single cells isolated by the original authors of the studies, each certifying compliance with local ethical committees and regulations. In one study[23], hepatocytes were isolated from six C57BL/6J mice (three aged 4 months and three aged 26 months). In another[38], MuSCs were isolated from six C57BL/6;DBA2 F1/JRj mice (three aged 1.5 months and three aged 26 months) and, in a third[28], embryos were collected from several female C57BL/6Babr mice.

Single-cell data processing. For the first study mentioned above[23], sequence data were downloaded from SRA with sratoolkit 2.10.8 under accession no. SRA344045. FASTQ files were pretrimmed before deposition to the SRA. Trimmed sequences were mapped to the mm10/GRCm38.p6 genome using Bismark 0.22.3 with the option *–non_directional*, as suggested by the Bismark User Guide v.0.21.0 for Zymo Pico-Methyl scWGBS library preparations. Reads were deduplicated, and methylation levels for CpG sites were extracted with Bismark[50].

For the studies of Hernando-Herraez et al.[38], Angermueller et al.[27], Smallwood et al.[25] and Argelaguet et al.[28], processed coverage files containing extracted methylation levels generated by Bismark were downloaded directly from the GEO database with GNU wget 1.17.1 under accession nos. GSE121436 (ref. [38]), GSE68642 (ref. [27]), GSE56879 (ref. [25]) and GSE121690 (ref. [28]), respectively.

All coverage files were then further processed to scale methylation level to a ratio between [0, 1]. While single-cell methylation profiles were almost entirely binary, technical considerations such as PCR amplification bias resulted in the presence of some intermediate methylation values. To address this, uncertain methylation calls of 0.5 were removed before downstream analysis and remaining methylation values were rounded to 0 or 1. Only genomic positions on the 19 mouse autosomes were retained for analysis. Coverage was interpreted as the total number of covered methylated and unmethylated cytosines in a CpG context on both DNA strands. Average global methylation in single cells was computed as the mean of all binary methylation states observed.

Due to the technical considerations of single-cell methylome sequencing, the number of CpGs covered in each cell is highly variable (Extended Data Fig. 9a). To maximize the numbers of cells for inclusion in our analysis and, while also filtering out low-quality dropout cells, we applied a coverage filter of at least 500,000 CpGs covered per cell, as previously done by others[38]. A summary of the single-cell datasets used, their accessions and the final cell types and numbers analyzed is provided in Supplementary Table 1.

Bulk data processing. To power the predictive capacity of *scAge*, we created bulk reference datasets that estimate the relationship between age and methylation level for a large set of CpGs. We downloaded processed bulk RRBS data from the study of Thompson et al. deposited in the GEO database under accession no. GSE120132 (ref. [34]). This dataset consists of 549 samples from liver, lung, blood, kidney, adipose and muscle tissues with age ranging from 1 to 21 months across three strains of mice. Since most single-cell datasets we analyzed were composed of cells from C57BL/6J or related mice, we exclusively isolated samples from this strain, resulting in 196 samples across six tissues with roughly equal tissue and age distributions. These samples formed the basis of the multi-tissue reference dataset. From this group, we selected tissue-specific samples for liver, blood and muscle, each with a consistent age distribution from young to old (Extended Data Fig. 1).

Methylation fractions in the bulk data were taken as the number of reads supporting a methylated status for a CpG over the total number of reads that covered this cytosine. To maximize the accuracy of bulk methylation levels while also preserving as many sites as possible, only CpG sites for which 90% of samples had at least fivefold coverage were retained[33]. This resulted in a final multi-tissue matrix of 196 samples across 748,955 positive-strand CpGs on autosomic chromosomes, with some missing values. Of note, the authors of the study by Thompson et al.[34] concatenated negative-strand CpG information to the positive strand, explaining why only positive-strand CpGs formed the basis of our training datasets. From this multi-tissue dataset, we created tissue-specific matrices for liver, blood and muscle tissues. We applied dimensionality reduction via principal component analysis (PCA) on all CpG sites to identify and remove outlier samples in single-tissue datasets. This also confirmed that tissue identity is the main component of variance in bulk methylation data (Extended Data Fig. 1b). We created filtered liver-, blood- and muscle-specific DNA methylation matrices containing 29 liver samples, 50 blood samples and 24 muscle samples with ages ranging from 2 to 21 months based on the same set of 748,955 positive-strand CpGs, as well as a multi-tissue matrix based on 196 samples across six tissues.

The *scAge* framework. To devise an algorithm to ascertain epigenetic age in single cells, we were inspired by recently published age predictors of individual bisulfite-barcoded-amplicon sequencing reads from bulk samples[3,7]. To begin, we used multi-tissue and tissue-specific methylation matrices to compute linear regression equations and Pearson correlations between methylation level and age for each CpG. These equations were in the form:

$$f_{\mathrm{CpG}}(age) = \mathrm{Met} = m_{\mathrm{CpG}} * age + b_{\mathrm{CpG}}$$

where *age* is treated as the independent variable predicting methylation (Met), and *m* and *b* are the slope and intercept of the CpG-specific regression line, respectively. This enabled the creation of reference linear association metrics between methylation level and age for each CpG covered in the training datasets (Fig. 1c).

Next, we intersected binarized methylation profiles of single cells with the reference data, producing a set of *N* common CpGs shared across both datasets (Fig. 1c). For each cell, we filtered these *N* CpGs based on the absolute value of their Pearson correlation with age, selecting the most age-associated CpGs in every cell. We evaluated several options to perform this selection. On the one hand, a specific number *n* of CpGs sites can be chosen for every cell. However, since coverage can vary widely among single cells, we instead opted to use a percentile-based approach: the top *x*% age-associated CpGs were selected per cell. We found that this enabled more consistent correlation distributions among single-cell profiles compared to an arbitrary number *n* of CpGs for every cell (Extended Data Fig. 6). Benchmarking revealed that single-tissue *scAge* clocks are most accurate when few, strongly age-associated CpGs are profiled (top 1%), while multi-tissue clocks improve in precision as slightly more CpGs are included (top 10%) (Extended Data Fig. 7). Due to this, we opted to use a top-1% age-associated CpGs cutoff in single-tissue predictions, and top-10% age-associated CpGs cutoff for multi-tissue predictions.

For each selected CpG per cell, we iterated through age in steps of 0.1 months from a minimum age to a maximum age parameter. In this work, we selected −20 and 60 months as the minimum and maximum values, respectively, to cover well past the lifespan of a typical mouse in both directions, and to prevent any computation bias in our predictions. These parameters may be changed when running the algorithm to any desired resolution and age range. Using the linear regression formula calculated per individual CpG in a training set, we computed the predicted methylation, $f_{CpG}(age)$ which, by the nature of the data, normally lies between 0 or 1. If this predicted value was outside of the range (0, 1), it was instead replaced by 0.001 or 0.999 depending on the proximity to either value. This ensured that predicted bulk methylation values were bounded in the unit interval, corresponding to a range between fully unmethylated (0) and fully methylated (1). Next, we assumed that the probability of observing a methylated single cell derived from a tissue of a given age was approximately equal to $f_{CpG}(age)$—that is, $Pr_{CpG}(age) = f_{CpG}(age)$. As an example, if a particular bulk tissue is 70% methylated (methylation, 0.7) at one CpG site, we expect that any random single cell from this tissue has a 70% chance of being methylated at that same CpG locus. Thus, the probability that a single cell was methylated at that CpG is $f_{CpG}(age)$ and, conversely, the probability that a single cell was not methylated at that CpG is $1 - f_{CpG}(age)$ (Fig. 1d). This provided an age-dependent probability for every common CpG retained in the algorithm. An important limitation to consider with this approach is that methylation distributions for some CpGs lie close to the boundaries of the unit interval, revealing truncated Gaussian distributions (Extended Data Fig. 2).

Assuming that all CpGs are independent from each other, the product of each of these probabilities will be the overall probability of the observed methylation pattern:

$$P(age) = \prod_{k=1}^{n} Pr_k(age)$$

where k represents individual CpGs (Fig. 1d,e). Our goal is then to find the maximum of that product among different ages (that is, to find the most probable age for observing a particular methylation pattern). Practically, we compute the sum across CpGs of the natural logarithm of the individual age-dependent probabilities, preventing underflow errors that result from large-scale fractional products. This gave us:

$$P(age) = \sum_{k=1}^{n} \ln(P_k(age))$$

for each age step. By harnessing the relationship of methylation level and age at many CpGs, these logarithmic sums ultimately provide a single likelihood metric for every age that a single cell comes from a bulk tissue of that age. Finally, we select the age of maximum likelihood as our predictor of epigenetic age for a single cell (Fig. 1e).

Single-cell profile simulations. To corroborate our findings, we investigated the capacity of *scAge* to profile epigenetic age in simulated single-cell profiles. For this, we used the 29 filtered bulk liver samples described above (Extended Data Fig. 1) and created ten simulated binary single-cell methylome profiles for each sample using a random Bernoulli distribution, with the probability parameter set to the bulk methylation level (Extended Data Fig. 10a). We observed that mean methylation patterns between simulated profiles and bulk data were consistent, despite shifting from a fractional to a binary data modality (Extended Data Fig. 10b). When we applied *scAge* to simulated profiles comprising the entire set of 748,955 CpGs in the bulk data, we observed strong predictive performance ($r = 0.96$) across all age groups with minimal variation between simulated cells (mean s.d. = 0.78; Extended Data Fig. 10c). To better account for the low and differential coverage observed in real single-cell profiles, we randomly downsampled these simulated profiles by a factor of ten and reran the *scAge* algorithm with identical parameters. This simulation similarly showed very strong predictive accuracy ($r = 0.96$), although prediction variance was increased as a result of random downsampling (mean s.d. = 1.36; Extended Data Fig. 10d).

Computational and statistical analyses. All analyses were performed using Python 3.9.2, running with *numpy* 1.20.2 and *pandas* 1.2.4 for mathematical computing. Figures were generated using *matplotlib* 3.4.1 in combination with *seaborn* 0.11.1. Welch's two-tailed *t*-test assuming unequal variances, implemented in *statannot* 0.2.3 and *scipy* 1.6.3, was used to perform statistical tests between groups. Two-tailed Pearson correlation analysis was also used for statistical tests. Bonferroni corrections were employed to correct for multiple testing where indicated.

Reporting Summary. Further information on research design is available in the Nature Research Reporting Summary linked to this article.

Data availability

All data used in this work were obtained from publicly available repositories. Processed single-cell coverage matrices were downloaded from GEO under the following accession nos.: GSE68642 (ref. [27]), GSE121436 (ref. [38]), GSE56879 (ref. [25]) and GSE121690 (ref. [28]). Trimmed sequencing files for the hepatocyte/MEF study were downloaded from the SRA under accession no. SRA344045 (ref. [23]). Bulk processed methylation data used for model training were downloaded from GEO under accession no. GSE120132 (ref. [34]).

Code availability

The *scAge* framework is publicly available at https://github.com/alex-trapp/scAge.

Received: 29 March 2021; Accepted: 29 September 2021;
Published online: 09 December 2021

References

1. Horvath, S. & Raj, K. DNA methylation-based biomarkers and the epigenetic clock theory of ageing. *Nat. Rev. Genet.* **19**, 371–384 (2018).
2. López-Otín, C., Blasco, M. A., Partridge, L., Serrano, M. & Kroemer, G. The hallmarks of aging. *Cell* **153**, 1194–1217 (2013).
3. Han, Y. et al. New targeted approaches for epigenetic age predictions. *BMC Biol.* **18**, 71 (2020).
4. Horvath, S. DNA methylation age of human tissues and cell types. *Genome Biol.* **14**, R115 (2013).
5. Lister, R. et al. Human DNA methylomes at base resolution show widespread epigenomic differences. *Nature* **462**, 315–322 (2009).
6. Meissner, A. et al. Reduced representation bisulfite sequencing for comparative high-resolution DNA methylation analysis. *Nucleic Acids Res.* **33**, 5868–5877 (2005).
7. Han, Y. et al. Targeted methods for epigenetic age predictions in mice. *Sci. Rep.* **10**, 22439 (2020).
8. Bocklandt, S. et al. Epigenetic predictor of age. *PLoS ONE* **6**, e14821 (2011).
9. Han, Y. et al. Epigenetic age-predictor for mice based on three CpG sites. *eLife* **7**, e37462 (2018).
10. Hannum, G. et al. Genome-wide methylation profiles reveal quantitative views of human aging rates. *Mol. Cell* **49**, 359–367 (2013).
11. Petkovich, D. A. et al. Using DNA methylation profiling to evaluate biological age and longevity interventions. *Cell Metab.* **25**, 954–960 (2017).
12. Meer, M. V., Podolskiy, D. I., Tyshkovskiy, A. & Gladyshev, V. N. A whole lifespan mouse multi-tissue DNA methylation clock. *eLife* **7**, e40675 (2018).
13. Levine, M. E. et al. An epigenetic biomarker of aging for lifespan and healthspan. *Aging* **10**, 573–591 (2018).
14. Lu, A. T. et al. DNA methylation GrimAge strongly predicts lifespan and healthspan. *Aging* **11**, 303–327 (2019).
15. Belsky, D. W. et al. Quantification of the pace of biological aging in humans through a blood test, the DunedinPoAm DNA methylation algorithm. *eLife* **9**, e54870 (2020).
16. Mammalian Methylation Consortium. Universal DNA methylation age across mammalian tissues. Preprint at *bioRxiv* https://doi.org/10.1101/2021.01.18.426733 (2021).
17. Lu, Y. et al. Reprogramming to recover youthful epigenetic information and restore vision. *Nature* **588**, 124–129 (2020).
18. Gill, D. et al. Multi-omic rejuvenation of human cells by maturation phase transient reprogramming. Preprint at *bioRxiv* https://doi.org/10.1101/2021.01.15.426786 (2021).
19. Bell, C. G. et al. DNA methylation aging clocks: challenges and recommendations. *Genome Biol.* **20**, 249 (2019).
20. Olova, N., Simpson, D. J., Marioni, R. E. & Chandra, T. Partial reprogramming induces a steady decline in epigenetic age before loss of somatic identity. *Aging Cell* **18**, e12877 (2019).
21. Sarkar, T. J. et al. Transient non-integrative expression of nuclear reprogramming factors promotes multifaceted amelioration of aging in human cells. *Nat. Commun.* **11**, 1545 (2020).
22. Karemaker, I. D. & Vermeulen, M. Single-cell DNA methylation profiling: technologies and biological applications. *Trends Biotechnol.* **36**, 952–965 (2018).
23. Gravina, S., Dong, X., Yu, B. & Vijg, J. Single-cell genome-wide bisulfite sequencing uncovers extensive heterogeneity in the mouse liver methylome. *Genome Biol.* **17**, 150 (2016).
24. Almanzar, N. et al. A single-cell transcriptomic atlas characterizes ageing tissues in the mouse. *Nature* **583**, 590–595 (2020).
25. Smallwood, S. A. et al. Single-cell genome-wide bisulfite sequencing for assessing epigenetic heterogeneity. *Nat. Methods* **11**, 817–820 (2014).
26. Guo, H. et al. Single-cell methylome landscapes of mouse embryonic stem cells and early embryos analyzed using reduced representation bisulfite sequencing. *Genome Res.* **23**, 2126–2135 (2013).
27. Angermueller, C. et al. Parallel single-cell sequencing links transcriptional and epigenetic heterogeneity. *Nat. Methods* **13**, 229–232 (2016).
28. Argelaguet, R. et al. Multi-omics profiling of mouse gastrulation at single-cell resolution. *Nature* **576**, 487–491 (2019).
29. Clark, S. J. et al. scNMT-seq enables joint profiling of chromatin accessibility DNA methylation and transcription in single cells. *Nat. Commun.* **9**, 781 (2018).

30. Argelaguet, R. et al. MOFA+: a statistical framework for comprehensive integration of multi-modal single-cell data. *Genome Biol.* **21**, 111 (2020).
31. Angermueller, C., Lee, H. J., Reik, W. & Stegle, O. DeepCpG: accurate prediction of single-cell DNA methylation states using deep learning. *Genome Biol.* **18**, 67 (2017).
32. Kapourani, C.-A. & Sanguinetti, G. Melissa: Bayesian clustering and imputation of single-cell methylomes. *Genome Biol.* **20**, 61 (2019).
33. Stubbs, T. M. et al. Multi-tissue DNA methylation age predictor in mouse. *Genome Biol.* **18**, 68 (2017).
34. Thompson, M. J. et al. A multi-tissue full lifespan epigenetic clock for mice. *Aging* **10**, 2832–2854 (2018).
35. Zou, H. & Hastie, T. Regularization and variable selection via the elastic net. *J. R. Stat. Soc. Ser. B Stat. Methodol.* **67**, 301–320 (2005).
36. Xie, W., Baylin, S. B. & Easwaran, H. DNA methylation in senescence, aging and cancer. *Oncoscience* **6**, 291–293 (2019).
37. Wang, T. et al. Epigenetic aging signatures in mice livers are slowed by dwarfism, calorie restriction and rapamycin treatment. *Genome Biol.* **18**, 57 (2017).
38. Hernando-Herraez, I. et al. Ageing affects DNA methylation drift and transcriptional cell-to-cell variability in mouse muscle stem cells. *Nat. Commun.* **10**, 4361 (2019).
39. García-Prat, L. et al. Autophagy maintains stemness by preventing senescence. *Nature* **529**, 37–42 (2016).
40. Schwörer, S. et al. Epigenetic stress responses induce muscle stem-cell ageing by Hoxa9 developmental signals. *Nature* **540**, 428–432 (2016).
41. Novak, J. S. et al. Human muscle stem cells are refractory to aging. *Aging Cell* **20**, e13411 (2021).
42. Kerepesi, C., Zhang, B., Lee, S.-G., Trapp, A. & Gladyshev, V. N. Epigenetic clocks reveal a rejuvenation event during embryogenesis followed by aging. *Sci. Adv.* **7**, eabg6082 (2021).
43. Ficz, G. et al. FGF signaling inhibition in ESCs drives rapid genome-wide demethylation to the epigenetic ground state of pluripotency. *Cell Stem Cell* **13**, 351–359 (2013).
44. Gladyshev, V. N. The ground zero of organismal life and aging. *Trends Mol. Med.* **27**, 11–19 (2021).
45. Pijuan-Sala, B. et al. A single-cell molecular map of mouse gastrulation and early organogenesis. *Nature* **566**, 490–495 (2019).
46. Titus, A. J., Gallimore, R. M., Salas, L. A. & Christensen, B. C. Cell-type deconvolution from DNA methylation: a review of recent applications. *Hum. Mol. Genet.* **26**, R216–R224 (2017).
47. Houseman, E. A. et al. Reference-free deconvolution of DNA methylation data and mediation by cell composition effects. *BMC Bioinformatics* **17**, 259 (2016).
48. Schaum, N. et al. Ageing hallmarks exhibit organ-specific temporal signatures. *Nature* **583**, 596–602 (2020).
49. Rando, T. A. & Wyss-Coray, T. Asynchronous, contagious and digital aging. *Nat. Aging* **1**, 29–35 (2021).
50. Krueger, F. & Andrews, S. R. Bismark: a flexible aligner and methylation caller for Bisulfite-Seq applications. *Bioinformatics* **27**, 1571–1572 (2011).

Acknowledgements

We thank T. Fox and A. Ganguly for help with schematic figures. We thank M. Mariotti, A. Shindyapina, S. H. Yim, S.-G. Lee, D. Santesmasses, P. Griffin and Y. Hu for helpful discussions. This work was supported by NIA grants to V.N.G. The funders had no role in study design, data collection and analysis, decision to publish or preparation of the manuscript. Some figures were created with BioRender.com.

Author contributions

A.T. and C.K. conceptualized the single-cell age prediction algorithm and processed the training data. A.T. handled all single-cell data, developed the *scAge* framework and performed all analyses in the manuscript. A.T. and V.N.G. wrote and revised the manuscript with help from C.K. A.T. and V.N.G. conceived the study and V.N.G. supervised the work.

Competing interests

Brigham and Women's Hospital is the sole owner of a provisional patent application directed at this invention in which all authors are named inventors.

Additional information

Supplementary information The online version contains supplementary material available at https://doi.org/10.1038/s43587-021-00134-3.

Correspondence and requests for materials should be addressed to Vadim N. Gladyshev.

Peer review information *Nature Aging* thanks Alex Zhavoronkov, Danica Chen and Lenhard Rudolph for their contribution to the peer review of this work.

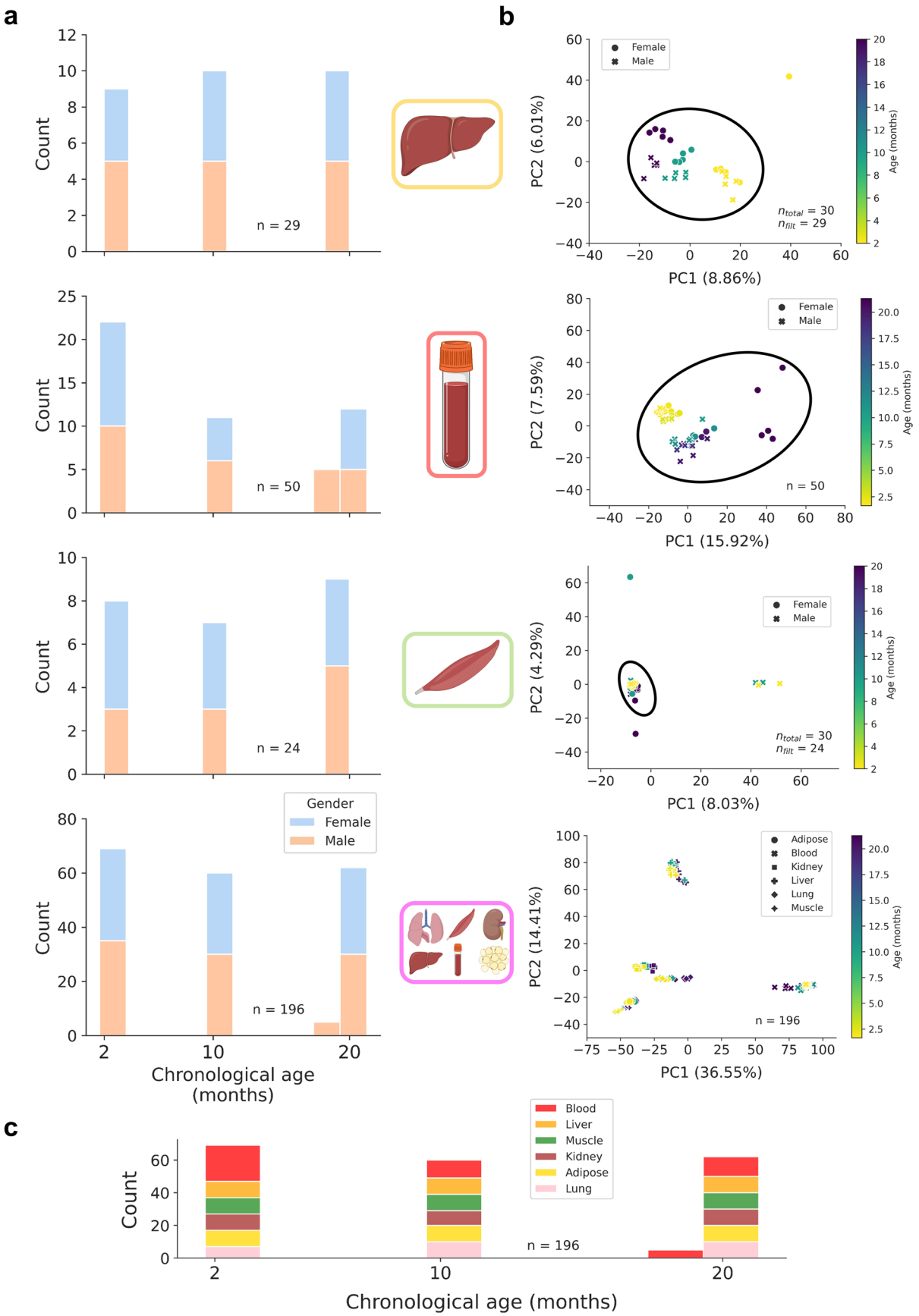

Extended Data Fig. 1 | See next page for caption.

Extended Data Fig. 1 | Bulk training data characteristics and dimensionality reduction. a) Age distributions for bulk training data in liver ($n = 29$), blood ($n = 50$), muscle ($n = 24$), and multi-tissue ($n = 196$) datasets, stratified by gender (female, blue; male, orange). **b**) Principal component analyses (PCA) across 748,955 CpG sites in liver, blood, muscle, and multi-tissue methylation matrices. For single-tissue datasets, black circles encompass samples that were retained for linear model training to exclude outliers and improve model accuracy. The number of samples before and after filtration is shown in the bottom right of each panel. Color scales depict the age in months of the animal (from young, yellow to old, purple). **c**) Age distribution in the multi-tissue dataset ($n = 196$), stratified by tissue type (blood, red; liver, orange; muscle, green; kidney, brown; adipose, yellow; lung, pink).

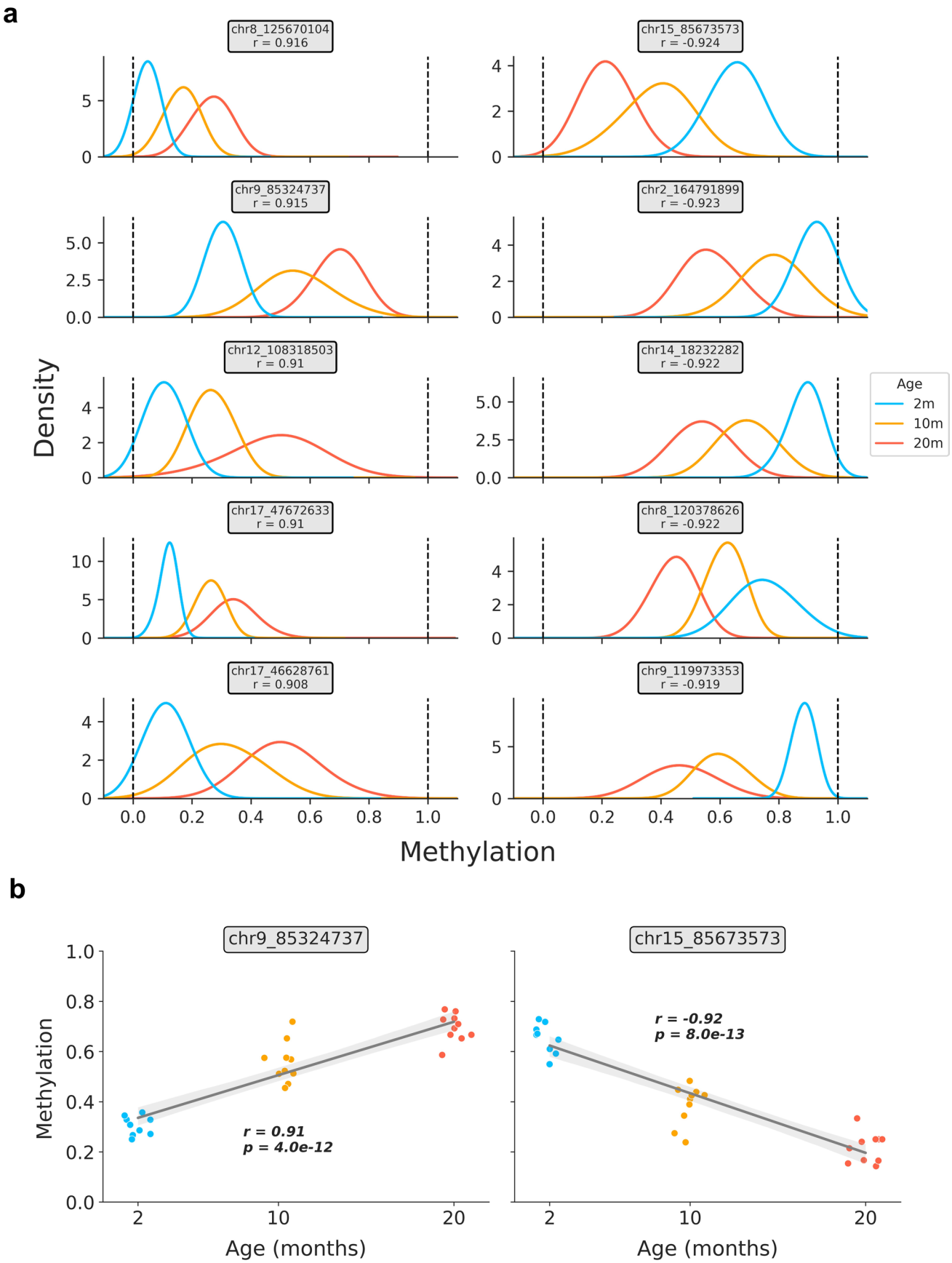

Extended Data Fig. 2 | See next page for caption.

Extended Data Fig. 2 | Relationship between age and bulk methylation level in age-associated CpG sites in liver. a) Kernel density estimation plots for the top 5 positively and negatively age-correlated CpG sites in the bulk liver data (based on $n = 29$ samples). CpG genomic positions are shown above each panel, along with the Pearson correlation coefficient (r) between methylation level and age. Colors correspond to the ages of mice (2 m, blue; 10 m, orange; 20 m, red). **b**) Representative scatterplots showing the relationship between age and methylation level in strongly positively (left) and negatively (right) age-associated CpG sites. Jitter was applied to the x-axis (age) purely for visualization purposes. Regression lines (grey) with 95% confidence intervals (light grey) are shown. Pearson correlation coefficients (r) and associated p-values (p) are shown. Two-tailed Pearson correlation analysis was employed for statistical testing, with statistics for each model treated independently without correction. Colors correspond to the ages of mice (2 m, blue; 10 m, orange; 20 m, red).

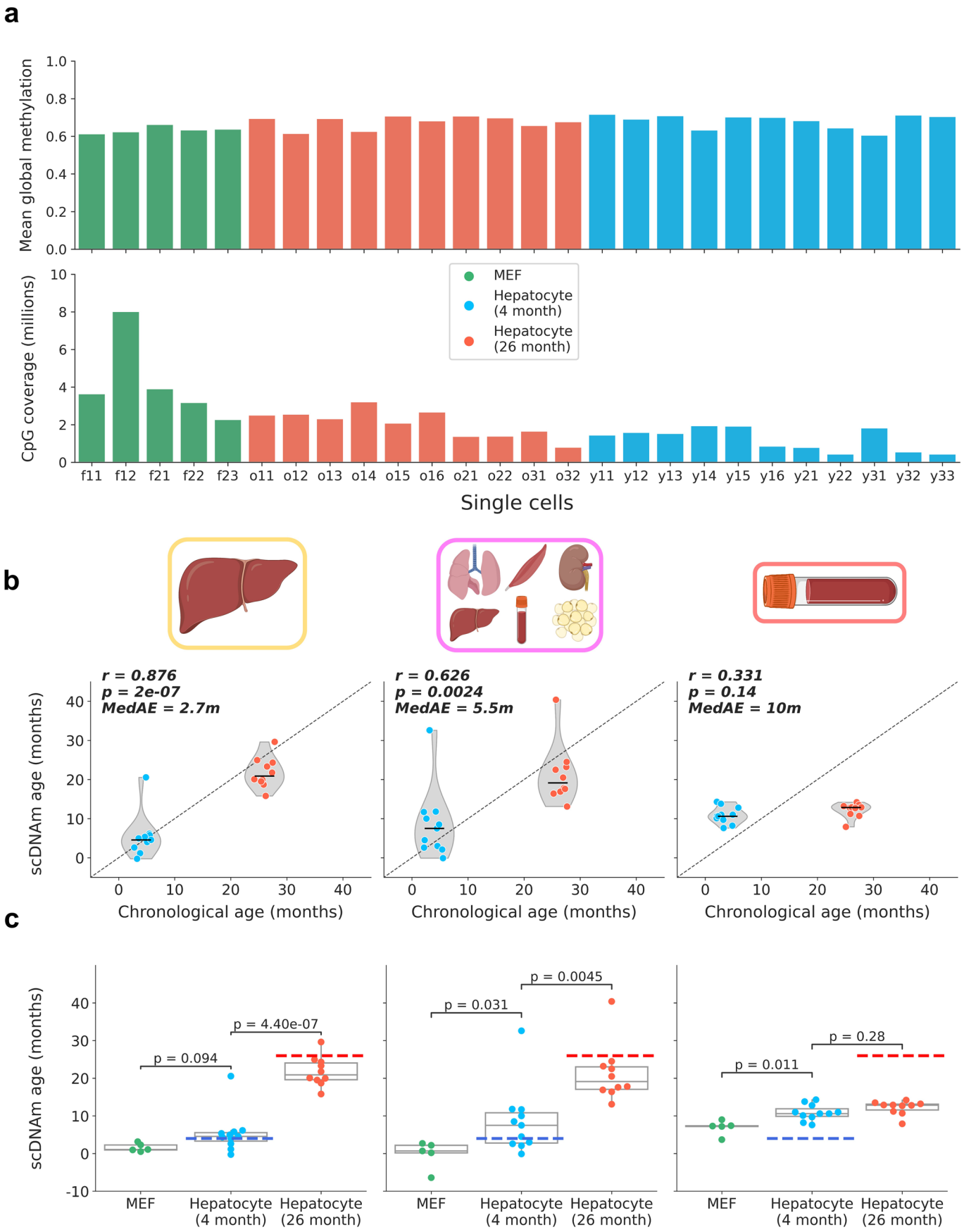

Extended Data Fig. 3 | See next page for caption.

Extended Data Fig. 3 | Global methylation, coverage, and scDNAm predictions in embryonic fibroblasts and hepatocytes with outliers. a) Bar plot of mean global methylation (top) and CpG coverage (bottom) in single mouse embryonic fibroblasts and hepatocytes. Each bar represents one cell. MEFs are shown in green, young hepatocytes in blue, and old hepatocytes in red. **b**) Predicted epigenetic age versus chronological age (top) in all young hepatocytes (blue, $n = 11$) and old hepatocytes (red, $n = 10$) across liver (left), multi-tissue (middle) and blood (right) models. Jitter was applied to x-axis (chronological age) strictly for visualization purposes. Pearson correlation (r), the associated p-value (p) and the median absolute error (*MedAE*) are shown. Two-tailed Pearson correlation analysis was employed for statistical testing with statistics for each model treated independently without correction. Violin plots show kernel density estimation of the data, with the median displayed by a black line. Further analysis of outliers is shown in Extended Data Fig. 5. Dots depict individual cells. **c**) Predicted epigenetic age, grouped by cell type, across liver (left), multi-tissue (middle) and blood (right) models for MEFs ($n = 5$, green), young hepatocytes ($n = 11$, blue), and old hepatocytes ($n = 10$, red). Two-tailed Welch's t-test was used for statistical testing, and Bonferroni correction was applied to correct for multiple testing. Box plots show median levels and the first and third quartile, whiskers show up to 1.5× the interquartile range. Dots depict individual cells.

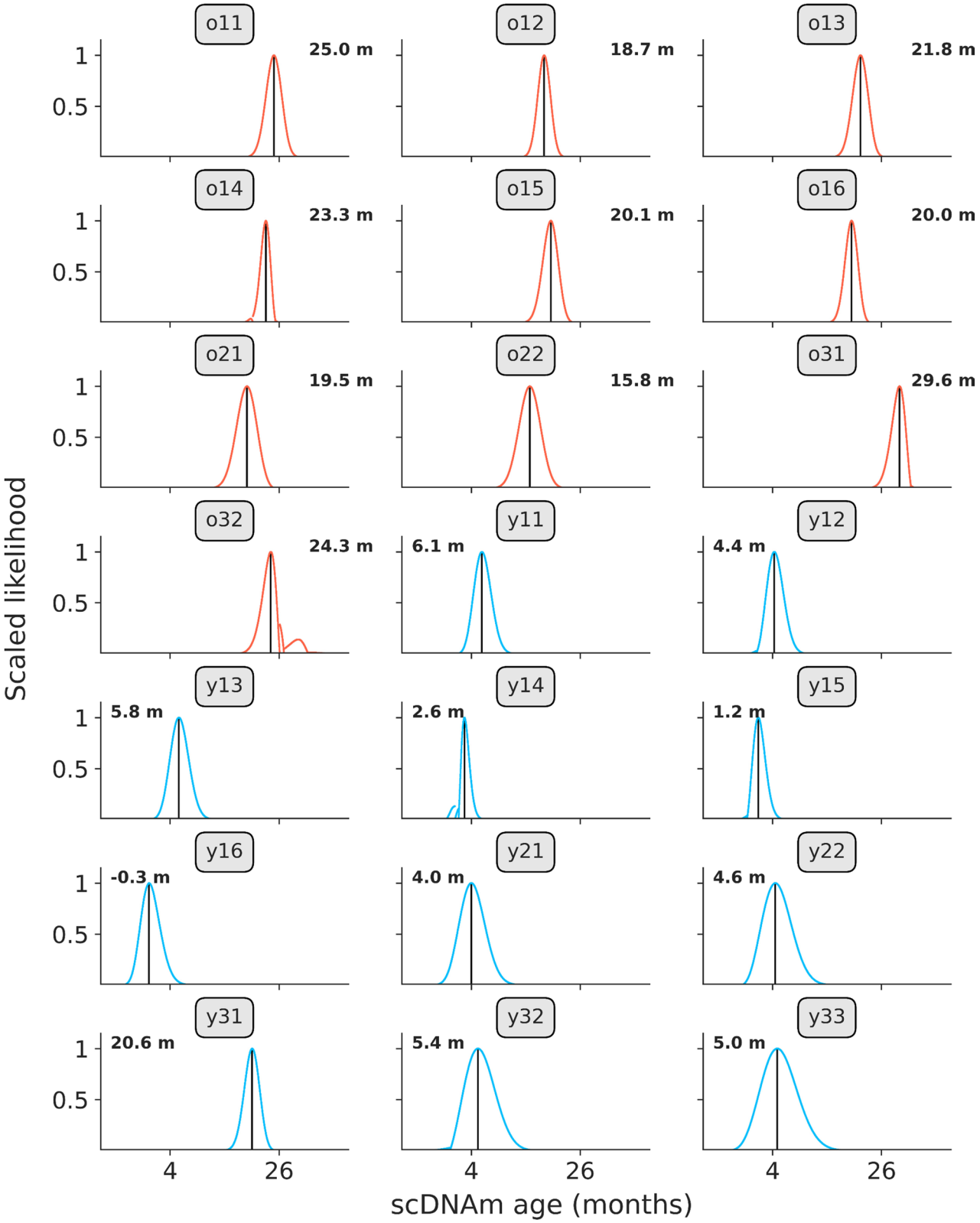

Extended Data Fig. 4 | Likelihood distributions in young and old hepatocytes. Likelihood distributions for all young (blue, $n=11$) and old (red, $n=10$) hepatocytes, based on scDNAm results from the liver model sampling the top 1% age-associated CpGs per cell. Black lines indicate age of maximum likelihood (predicted epigenetic age), which is depicted numerically in the top right or left corners of each panel. Labels indicate cell identifier, as given in the study metadata on the SRA. Likelihood was calculated by taking the exponential of the log-likelihood profiles, which was subsequently scaled between 0 and 1 to normalize distributions between cells.

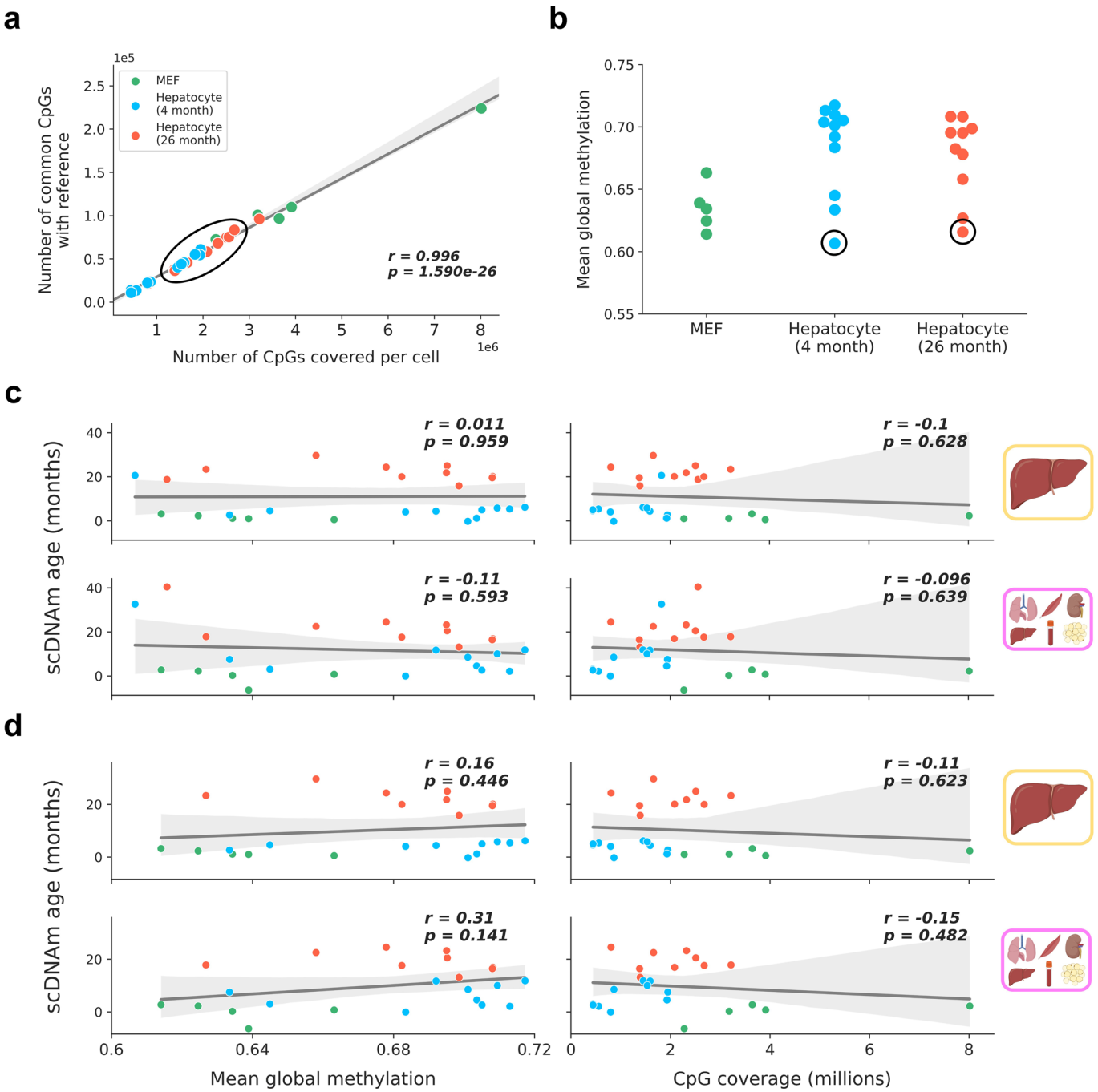

Extended Data Fig. 5 | Outlier analysis and lack of relationship between scDNAm age and technical covariates in hepatocytes and fibroblasts. a) Scatterplot depicting the strongly linear relationship between CpG coverage in a single cell (x-axis) and the number of CpGs intersecting with the liver training dataset (y-axis) for embryonic fibroblasts (green, $n=5$), young hepatocytes (blue, $n=11$) and old hepatocytes (red, $n=10$). Regression line (grey) is shown with a 95% confidence interval (light grey). Outlier samples based on scDNAm predictions and PCA analysis in the original study are within the black circle, highlighting these cells are not outliers in regard to CpG coverage. Pearson correlation coefficient (*r*) and the associated two-tailed p-value (*p*) are shown. **b**) Mean global methylation of embryonic fibroblasts (green, $n=5$), young (blue, $n=11$) and old hepatocytes (red, $n=10$). Outlier samples detected during dimensionality reduction and age predictions are circled in black. **c**, **d**) Scatterplots depicting the relationship of mean global methylation (left) and CpG coverage (right) with predicted epigenetic age (scDNAm age) for single embryonic fibroblasts ($n=5$, green) and hepatocytes (young, $n=11$, blue; old, $n=10$, red) across liver and multi-tissue datasets with the two outliers included (c) and with the two outliers excluded (d). Regression lines (grey) are shown with a 95% confidence interval (light grey). Two-tailed Pearson correlation analysis was used for statistical testing, with each analysis treated independently without correction. Pearson correlation coefficients (*r*) and associated two-tailed p-values (*p*) are shown. No significant relationship is observed in any comparison. The legend in panel (a) applies to all of the panels in this figure.

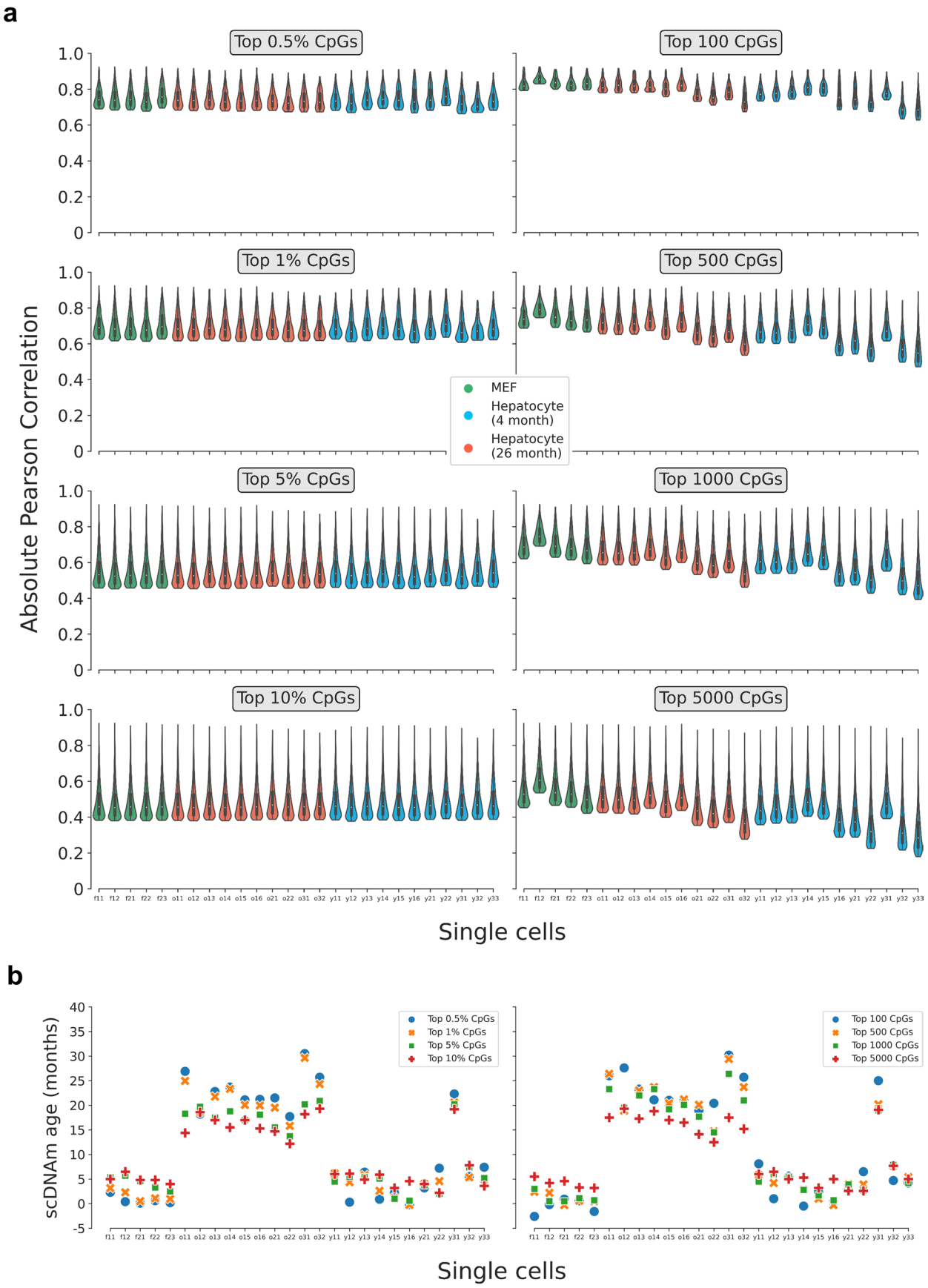

Extended Data Fig. 6 | See next page for caption.

Extended Data Fig. 6 | Pearson correlation distributions and predicted ages in single cells based on various CpG selection parameters. a) Violin plots depicting the distribution of the Pearson correlation coefficient of *scAge*-chosen CpGs in embryonic fibroblasts ($n = 5$, green) and hepatocytes (young, $n = 11$, blue; old, $n = 10$, red) based on the selection method. On the left, a percentile-based method is employed, wherein the top *x*% absolute age-associated CpGs are chosen in every cell. On the right, a defined number of CpGs is chosen across every cell, leading to more uneven distributions due to differential cell CpG coverage. Various parameters for both methods (grey boxes) and their effects on the distributions are shown. Violin plots depict kernel density estimations of the data. Inner boxplots depict median levels (white dot) and first and third quartiles, with whiskers extending up to 1.5x the interquartile range. The central legend applies to all subpanels in this panel. **b**) Predicted epigenetic ages using the liver model for all embryonic fibroblasts ($n = 5$) and hepatocytes (young, $n = 11$; old, $n = 10$), based on the selection method (left, percentile; right, defined number of CpGs) and parameter. Colors depict the % or number of CpGs chosen for *scAge* computations (top 0.5% or 100 CpGs, blue; top 1% or 500 CpGs, orange; top 5% or 1,000 CpGs, green; top 10% or 5,000 CpGs, red).

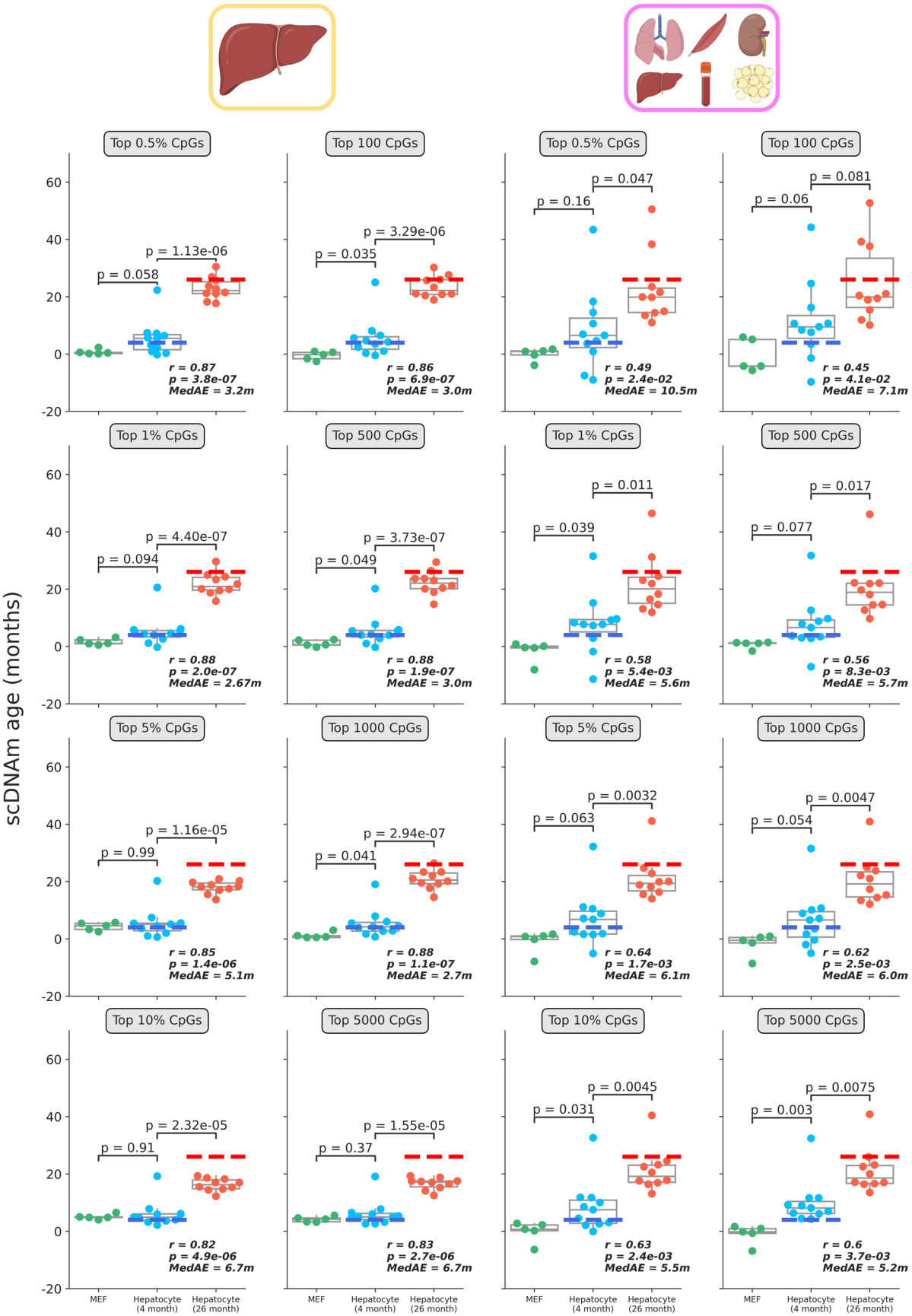

Extended Data Fig. 7 | See next page for caption.

Extended Data Fig. 7 | Single-cell epigenetic age predictions differ based on selection mode and training dataset. Predicted epigenetic ages in all embryonic fibroblasts (green, $n = 5$), young hepatocytes (blue, $n = 11$) and old hepatocytes (red, $n = 10$) using the liver model (left two columns) and multi-tissue models (right two columns) across different CpG selection modes and parameters. Parameters are labeled in grey boxes above the plots. Bonferroni corrections were applied to account for multiple testing. Pearson correlation (*r*), its associated p-value (*p*), and the median absolute error (*MedAE*) are shown for each panel. Two-tailed Pearson correlation analysis was employed for statistical testing. Dashed lines represent the chronological age of animals from which hepatocytes were obtained (4-months-old, dark blue; 26-months-old, dark red). Boxplots depict median levels and the first/third quartile, with whiskers extending up to 1.5x the interquartile range. Individual cells are depicted as points.

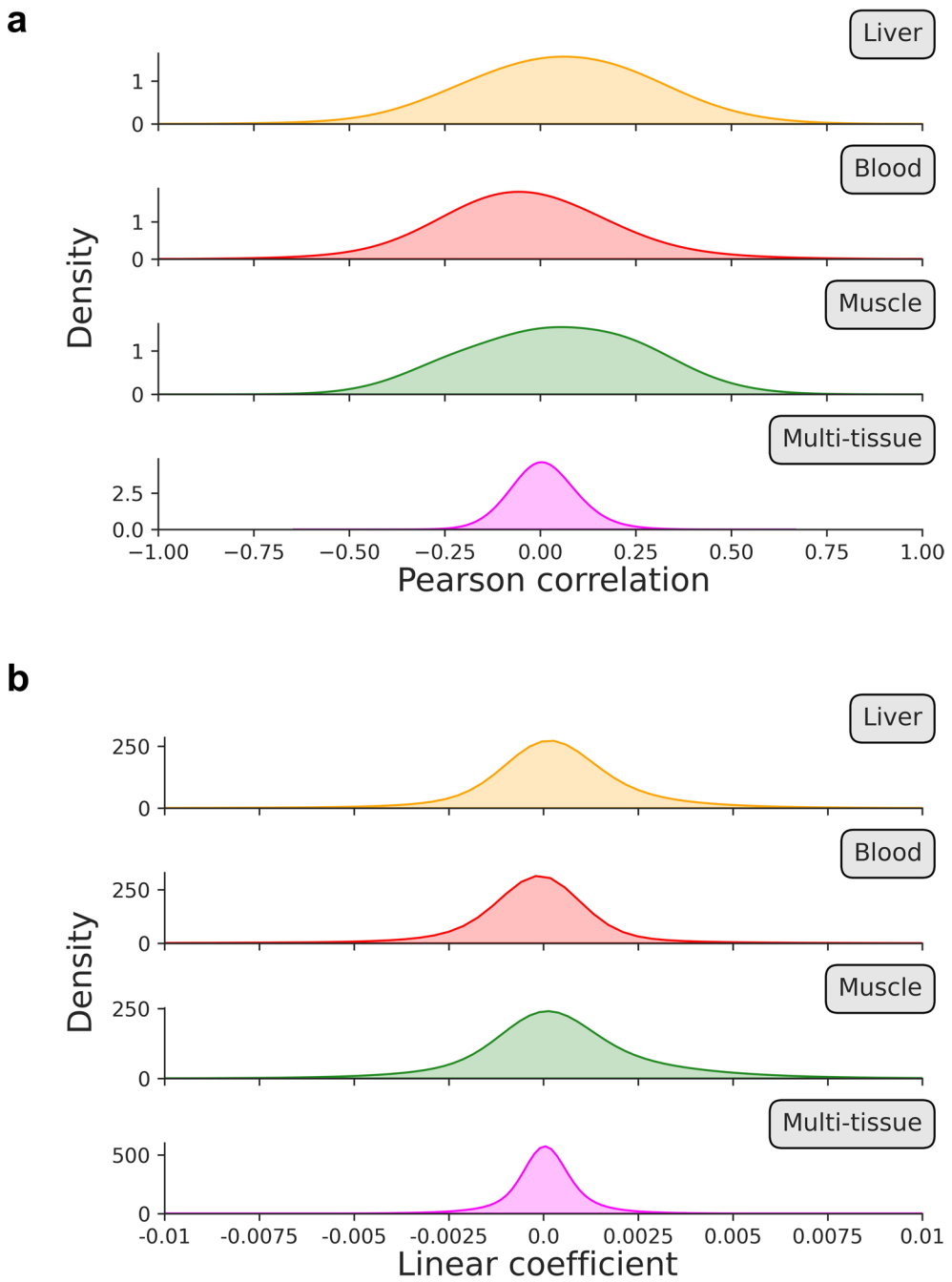

Extended Data Fig. 8 | Distribution of Pearson correlation coefficients and linear association metrics across training datasets. a, **b**) Kernel density estimation plots for (a) Pearson correlation coefficients and (b) linear regression coefficients in processed training reference data for liver (orange), blood (red), muscle (green), and multi-tissue (magenta) datasets. Individual distributions are labeled on the upper right side to indicate which tissue is depicted.

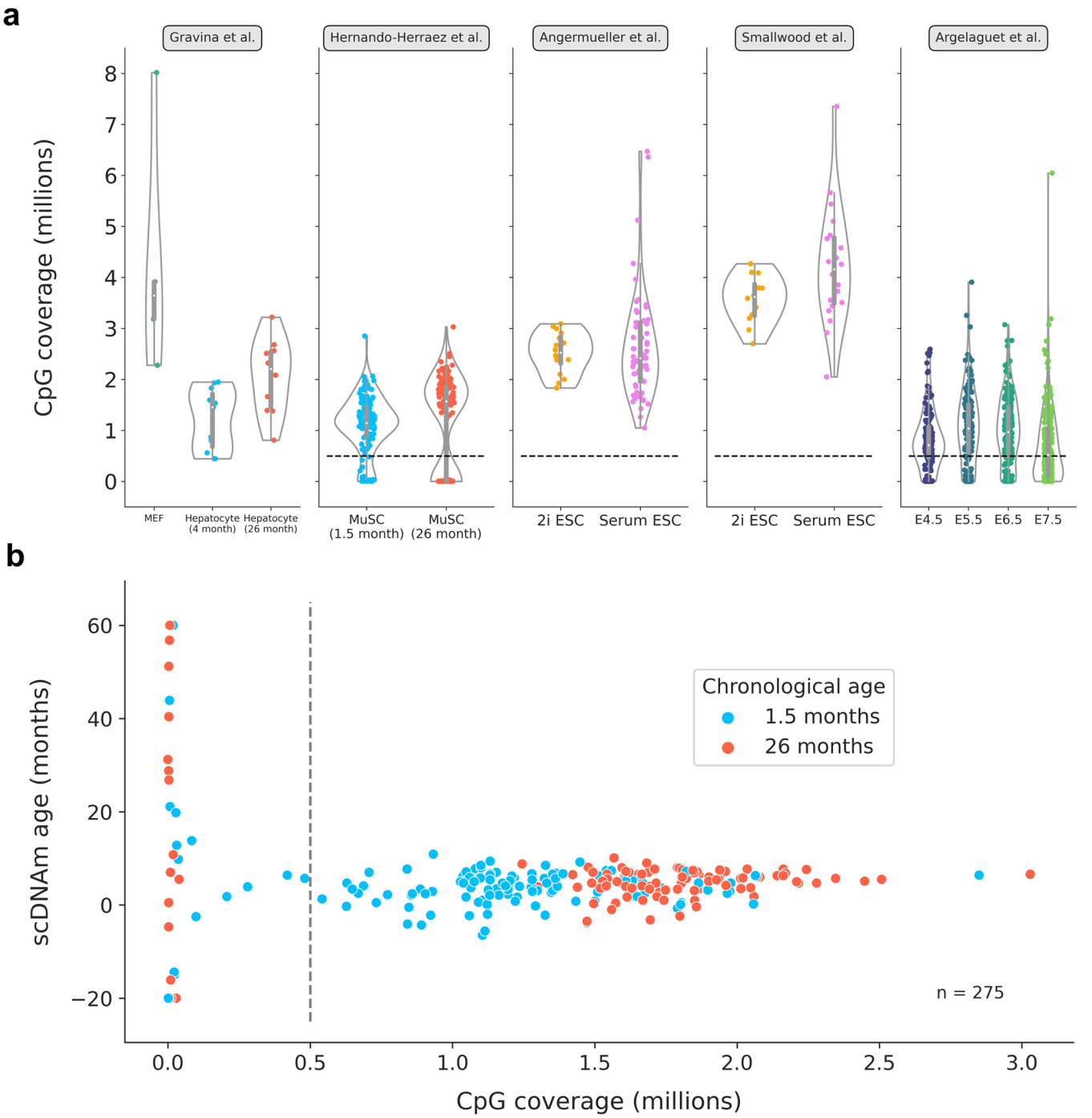

Extended Data Fig. 9 | Single-cell coverage distributions and the effect of coverage on *scAge* predictions. a) Distributions of single-cell CpG coverage across all 5 datasets analyzed in this study. Dotted lines represent the cutoff value that was used for downstream analysis (at least 500,000 CpGs per cell), in line with previous work[38]. Given the low sample size and relatively high coverage, no filtration was applied to cells from the Gravina et al. study[23]. The number of cells passing the filtration cutoff in each dataset is further detailed in Supplementary Table 1. Violin plots depict the kernel density estimation of the data. Inner boxplots depict the median (white dot), as well as the first/third quartile (grey box), with whiskers extending up to 1.5x the interquartile range. Individual dots depict single cells. Colors align with those presented in main figures (Gravina et al: MEFs in green; young hepatocytes in blue; old hepatocytes in red; Hernando-Herraez et al: young MuSCs in blue, old MuSCs in red; Angermueller et al and Smallwood et al: 2i ESCs in yellow, serum ESCs in pink; Argelaguet et al: E4.5 cells in purple, E5.5 cells in dark blue, E6.5 cells in dark green, E7.5 cells in light green). **b**) Scatterplot depicting the relationship between CpG coverage and predicted epigenetic ages in all unfiltered muscle stem cells[38] ($n = 275$). Dotted black line represents the cutoff of 500,000 CpGs per cell, after which predictions greatly stabilize. MuSCs from young animals are shown in blue, and those from old animals are shown in red.

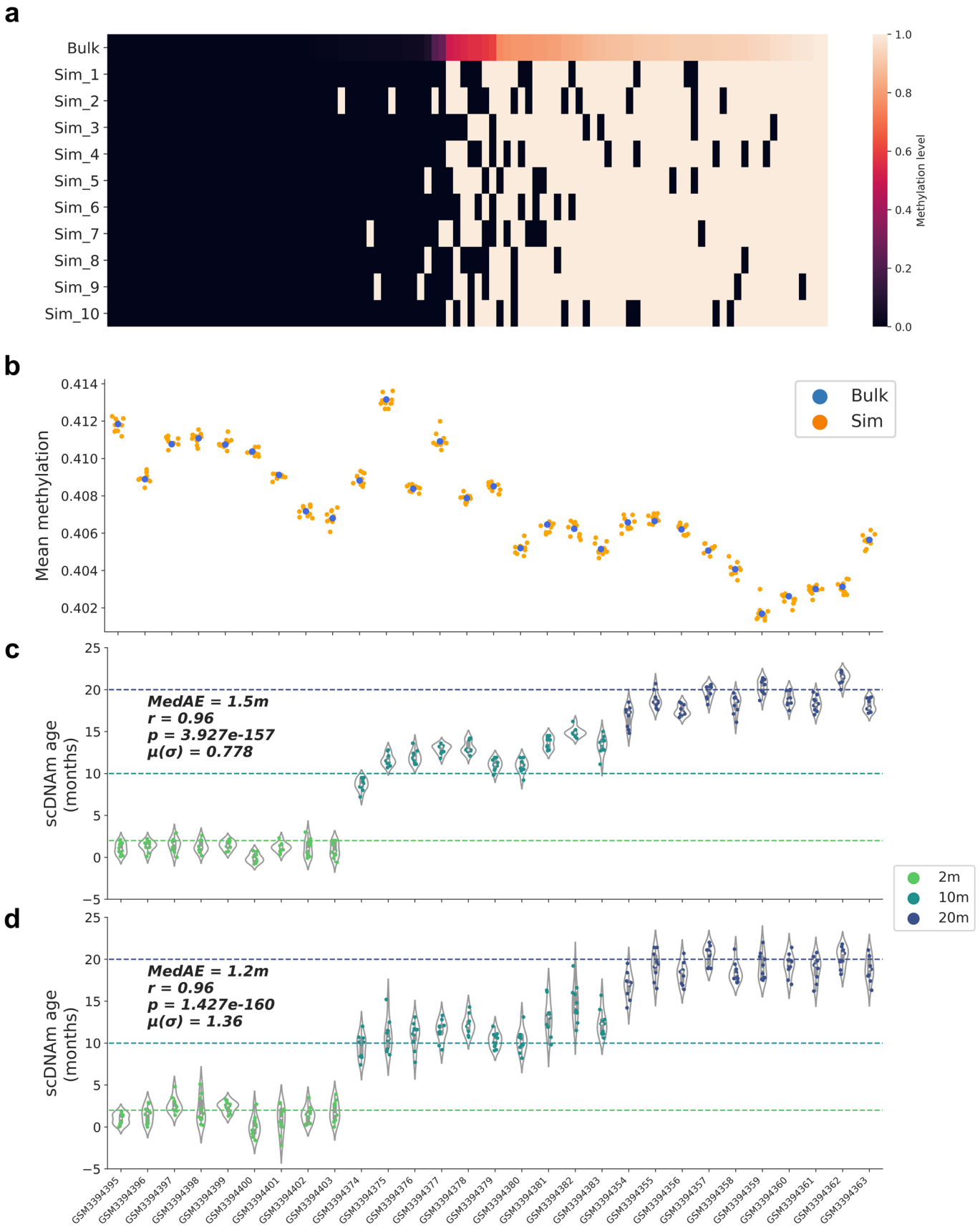

Extended Data Fig. 10 | See next page for caption.

Extended Data Fig. 10 | Single-cell profile simulations and epigenetic age predictions. a) Heatmap of methylation values in bulk and simulated single-cell profiles. 100 CpGs were randomly selected from a bulk liver sample[34], and random Bernoulli distributions were used to generate 10 simulated binary profiles per bulk sample. As the bulk methylation level (top) of CpGs increases from left to right, more simulated single-cell profiles are methylated as opposed to unmethylated. Color scale depicts methylation level from unmethylated (0, black) to methylated (1, white). **b**) Mean global methylation of bulk samples (blue) and 10 simulated full binary profiles per sample (orange) across 29 bulk liver RRBS samples, arranged from young (left) to old (right). Simulated binary profiles cluster with their bulk source, despite shifting from a fractional to a binary data modality. **c**, **d**) Predicted epigenetic age for each simulated binary profile with (c) full coverage of 748,955 CpGs per simulated profile and (d) randomly 10x downsampled coverage of 74,896 distinct CpGs per simulated profile. Profiles are arranged from young (left) to old (right). Age of the animals is denoted by the color of the points (2 m, light green; 10 m, dark green; 20 m, dark blue). Two-tailed Pearson correlation analysis was employed for statistical testing, with statistics for each simulation treated independently without correction. The Pearson correlation coefficient (*r*), the associated two-tailed p-value (*p*), median absolute error (*MedAE*) and mean of the standard deviations for each sample ($\mu(\sigma)$) are shown. Violin plots in (c) and (d) depict the kernel density estimation of the data. Inner boxplots depict the median (white dot), as well as the first/third quartile (grey box), with whiskers extending up to 1.5x the interquartile range. Individual dots depict simulated single cell profiles.

nature portfolio

Corresponding author(s): Vadim N. Gladyshev

Last updated by author(s): Sep 15, 2021

Reporting Summary

Nature Portfolio wishes to improve the reproducibility of the work that we publish. This form provides structure for consistency and transparency in reporting. For further information on Nature Portfolio policies, see our Editorial Policies and the Editorial Policy Checklist.

Statistics

For all statistical analyses, confirm that the following items are present in the figure legend, table legend, main text, or Methods section.

n/a	Confirmed
☐	☒ The exact sample size (*n*) for each experimental group/condition, given as a discrete number and unit of measurement
☐	☒ A statement on whether measurements were taken from distinct samples or whether the same sample was measured repeatedly
☐	☒ The statistical test(s) used AND whether they are one- or two-sided *Only common tests should be described solely by name; describe more complex techniques in the Methods section.*
☐	☒ A description of all covariates tested
☐	☒ A description of any assumptions or corrections, such as tests of normality and adjustment for multiple comparisons
☐	☒ A full description of the statistical parameters including central tendency (e.g. means) or other basic estimates (e.g. regression coefficient) AND variation (e.g. standard deviation) or associated estimates of uncertainty (e.g. confidence intervals)
☐	☒ For null hypothesis testing, the test statistic (e.g. *F*, *t*, *r*) with confidence intervals, effect sizes, degrees of freedom and *P* value noted *Give P values as exact values whenever suitable.*
☒	☐ For Bayesian analysis, information on the choice of priors and Markov chain Monte Carlo settings
☒	☐ For hierarchical and complex designs, identification of the appropriate level for tests and full reporting of outcomes
☐	☒ Estimates of effect sizes (e.g. Cohen's *d*, Pearson's *r*), indicating how they were calculated

Our web collection on statistics for biologists contains articles on many of the points above.

Software and code

Policy information about availability of computer code

Data collection	Trimmed FASTQ files for the Gravina et al. study were downloaded from the SRA using sratoolkit 2.10.8. Remaining methylation data (processed coverage files and bulk training data) were available from GEO as supplementary files and were downloaded using GNU Wget 1.17.1.
Data analysis	The scAge framework developed and used throughout this manuscript is available at https://github.com/alex-trapp/scAge. Analysis was conducted with Python 3.9.2. Plotting was performed with the matplotlib 3.4.1 and seaborn 0.11.1 packages, in conjunction with statannot 0.2.3. The packages scipy 1.6.3 and sklearn 0.24.2 were also used to compute correlations and linear regression models. Computations and data representations were made possible with numpy 1.20.2 and pandas 1.2.4. Sequencing reads for the Gravina et al. study were processed with Bismark 0.22.3.

For manuscripts utilizing custom algorithms or software that are central to the research but not yet described in published literature, software must be made available to editors and reviewers. We strongly encourage code deposition in a community repository (e.g. GitHub). See the Nature Portfolio guidelines for submitting code & software for further information.

Data

Policy information about availability of data

All manuscripts must include a data availability statement. This statement should provide the following information, where applicable:

- Accession codes, unique identifiers, or web links for publicly available datasets
- A description of any restrictions on data availability
- For clinical datasets or third party data, please ensure that the statement adheres to our policy

All data used in this work was obtained from publicly available repositories. Processed single-cell coverage matrices were downloaded from GEO under the

following accessions: GSE68642, GSE121436, GSE56879, and GSE121690. Trimmed sequencing files for the Gravina et al. study were downloaded from the SRA, under accession SRA344045. Bulk methylation data used for model training was downloaded from GEO under accession GSE120132.

Field-specific reporting

Please select the one below that is the best fit for your research. If you are not sure, read the appropriate sections before making your selection.

☒ Life sciences ☐ Behavioural & social sciences ☐ Ecological, evolutionary & environmental sciences

For a reference copy of the document with all sections, see nature.com/documents/nr-reporting-summary-flat.pdf

Life sciences study design

All studies must disclose on these points even when the disclosure is negative.

Sample size	Sample sizes were determined and justified in the original studies that we analyzed throughout this manuscript (Gravina et al., 2016; Angermueller et al., 2016; Smallwood et al., 2014; Hernando-Herraez et al., 2019; Argelaguet et al., 2019). All relevant single-cell methylation data from these studies were analyzed.
Data exclusions	Cells with CpG coverage less than 500,000 were excluded from the final age prediction analyses to remove dropout cells with aberrant predictions. This exclusion criteria was not pre-established, but we followed earlier guidelines from Hernando-Herraez et al., 2019, where the authors also discarded low-quality cells with fewer than 500,000 CpGs covered. We discuss in detail the effect of CpG coverage on single-cell DNAm predictions in the muscle stem cell section in the Results and in Extended Data Fig. 9.
Replication	Replication determinations were made in the original studies (Gravina et al., 2016; Angermueller et al., 2016; Smallwood et al., 2014; Hernando-Herraez et al., 2019; Argelaguet et al., 2019). We analyzed all relevant data, ranging from a minimum of 5 replicates (embryonic fibroblasts, Gravina et al.) to a maximum of 155 replicates (E7.5 embryonic cells, Argelaguet et al.).
Randomization	No allocation into experimental/control groups was performed in any of the studies that we analyzed (Gravina et al., 2016; Angermueller et al., 2016; Smallwood et al., 2014; Hernando-Herraez et al., 2019; Argelaguet et al., 2019). Randomization was thus not relevant for this manuscript.
Blinding	No allocation into experimental/control groups was performed in any of the studies that we analyzed (Gravina et al., 2016; Angermueller et al., 2016; Smallwood et al., 2014; Hernando-Herraez et al., 2019; Argelaguet et al., 2019). Neither we nor the authors of the studies mentioned were blinded to the identity of the cells or the age of the animals in any of the studies. This information was made available in public metadata.

Reporting for specific materials, systems and methods

We require information from authors about some types of materials, experimental systems and methods used in many studies. Here, indicate whether each material, system or method listed is relevant to your study. If you are not sure if a list item applies to your research, read the appropriate section before selecting a response.

Materials & experimental systems

n/a	Involved in the study
☒	☐ Antibodies
☒	☐ Eukaryotic cell lines
☒	☐ Palaeontology and archaeology
☒	☐ Animals and other organisms
☒	☐ Human research participants
☒	☐ Clinical data
☒	☐ Dual use research of concern

Methods

n/a	Involved in the study
☒	☐ ChIP-seq
☒	☐ Flow cytometry
☒	☐ MRI-based neuroimaging